Crystallographic and Kinetic Studies of Human Mitochondrial Acetoacetyl-CoA Thiolase: The Importance of Potassium and Chloride Ions for Its Structure and Function[†,‡]

Antti M. Haapalainen,[§,||] Gitte Meriläinen,[§,||] Päivi L. Pirilä,[§] Naomi Kondo,[⊥] Toshiyuki Fukao,[⊥] and Rik K. Wierenga*[,§]

Biocenter Oulu and Department of Biochemistry, University of Oulu, P.O. Box 3000, FIN-90014 Oulu, Finland, and Department of Pediatrics, Graduate School of Medicine, Gifu University, Yanagidol-1, Gifu 501-1194, Japan

Received December 20, 2006; Revised Manuscript Received February 7, 2007

ABSTRACT: Thiolases are CoA-dependent enzymes which catalyze the formation of a carbon−carbon bond in a Claisen condensation step and its reverse reaction via a thiolytic degradation mechanism. Mitochondrial acetoacetyl-coenzyme A (CoA) thiolase (T2) is important in the pathways for the synthesis and degradation of ketone bodies as well as for the degradation of 2-methylacetoacetyl-CoA. Human T2 deficiency has been identified in more than 60 patients. A unique property of T2 is its activation by potassium ions. High-resolution human T2 crystal structures are reported for the apo form and the CoA complex, with and without a bound potassium ion. The potassium ion is bound near the CoA binding site and the catalytic site. Binding of the potassium ion at this low-affinity binding site causes the rigidification of a CoA binding loop and an active site loop. Unexpectedly, a high-affinity binding site for a chloride ion has also been identified. The chloride ion is copurified, and its binding site is at the dimer interface, near two catalytic loops. A unique property of T2 is its ability to use 2-methyl-branched acetoacetyl-CoA as a substrate, whereas the other structurally characterized thiolases cannot utilize the 2-methylated compounds. The kinetic measurements show that T2 can degrade acetoacetyl-CoA and 2-methylacetoacetyl-CoA with similar catalytic efficiencies. For both substrates, the turnover numbers increase approximately 3-fold when the potassium ion concentration is increased from 0 to 40 mM KCl. The structural analysis of the active site of T2 indicates that the Phe325-Pro326 dipeptide near the catalytic cavity is responsible for the exclusive 2-methyl-branched substrate specificity.

Thiolases are ubiquitous and important enzymes. Several isoenzymes are known, which can occur in the cytosol, the mitochondria, or the peroxisomes (*1*). Thiolases function in both degradative and synthetic pathways. In the degradative direction, thiolases catalyze the thiolytic cleavage of 3-ketoacyl-CoA[1] molecules, which is an important step of the β-oxidation pathway of fatty acid degradation. In the synthetic direction, a Claisen condensation reaction is catalyzed, by which acetoacetyl-CoA is synthesized from two molecules of acetyl-CoA (Figure 1A). The degradative thiolases have a broad chain length specificity and are also termed 3-ketoacyl-CoA thiolases (EC 2.3.1.16), while the synthetic thiolases (EC 2.3.1.9), which can use only short chain fatty acyl-CoA molecules (maximally up to C4), are also known as acetoacetyl-CoA thiolases. There is a high degree of sequence similarity between these two thiolase classes. Some thiolases are dimers, but most thiolases are tetramers (*2*). In mammals, two synthetic thiolases have been identified, the cytosolic acetoacetyl-CoA thiolase (CT) and the mitochondrial acetoacetyl-CoA thiolase (T2), both of which are tetrameric enzymes.

Thiolase activity was first described in 1951 by Lynen and co-workers, as reviewed by Lynen and Gehring (*3*). The first purified thiolase was pig heart thiolase, now usually called T2 (*4*, *5*). Studies on rat T2 showed that its thiolytic activity was activated by potassium ions but not by sodium ions (*6*, *7*). A unique catalytic property of T2 concerns its substrate specificity, as its active site also catalyzes the degradation of 2-methylacetoacetyl-CoA (*8*), which is an important intermediate in the catabolic pathway of isoleucine and methylated fatty acids branched at even-numbered

[†] This study has been supported by Academy of Finland Grant 200966 and by Biocenter Oulu. Support from the "European Community-Research Infrastructure Action under the FP6" structuring the "European Research Area Programme" through Contract RII3/CT/2004/5060008 (to EMBL/DESY) and through the "Integrated Infrastructure Initiative-Integrating Activity on Synchrotron and Free Electron Laser Science" (to MAX-lab) is acknowledged.

[‡] The coordinates and structure factors have been deposited at the RCSB Protein Data Bank as entries (Table 1) 2IB7 (RCSB039366) for apoT2, 2IB8 (RCSB039367) for apoT2+KCl, 2IB9 (RCSB039368) for apoT2+KCl(ano), 2IBU (RCSB039389) for T2+CoA, 2IBW (RCSB039391) for T2+CoA+KCl, and 2IBY (RCSB039393) for T2+CoA+KNO_3.

* To whom correspondence should be addressed. E-mail: Rik.Wierenga@oulu.fi. Telephone: +358 8 553 1199. Fax: +358 8 553 1141.

[§] University of Oulu.

[||] These authors contributed equally to this paper.

[⊥] Gifu University.

[1] Abbreviations: CoA, coenzyme A; T2, mitochondrial acetoacetyl-CoA thiolase; CT, cytosolic acetoacetyl-CoA thiolase; bCT, bacterial CT; hCT, human CT.

10.1021/bi6026192 CCC: $37.00
Published on Web 03/20/2007

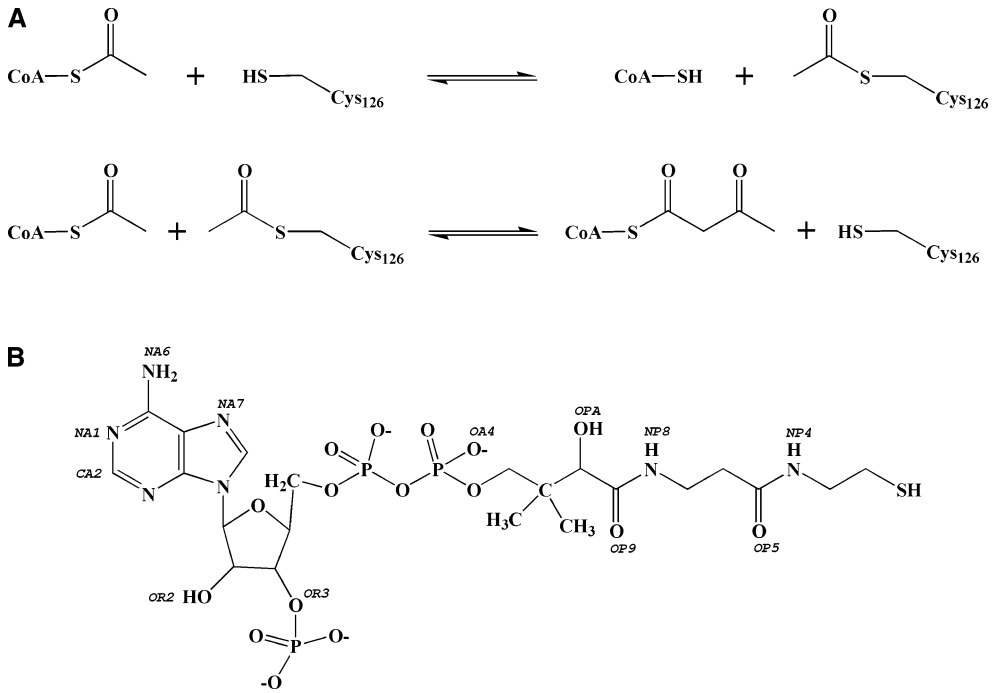

FIGURE 1: (A) Claisen condensation reaction, as catalyzed by T2. In the first part of the reaction cycle, the catalytic cysteine, Cys126, becomes acetylated. During the second part of the cycle, another acetyl-CoA binds to the active site and acetoacetyl-CoA is released. (B) Covalent structure of CoA. The labeled atoms are discussed in the text; these atoms have hydrogen bonding interactions with T2 or with waters.

carbons. T2 is present in most tissues and abundant in liver, kidney, heart, brain, and adrenal gland (*9*).

Several inborn errors related to sequence changes in thiolase genes have been found (*10*−*12*). T2 deficiency is known to affect both the isoleucine catabolism and the ketone body metabolism. Ketone body metabolism concerns the synthesis of acetoacetate and 3-hydroxybutyrate in the liver and their subsequent degradation in the extrahepatic tissues. This metabolic pathway is in fact an important energy supply for the brain and heart. The major clinical manifestation of T2 deficiency is related to its intermittent ketoacidosis and urinary excretion of large amounts of ketone bodies, acetoacetate, and 3-hydroxybutyrate, as well as compounds of the isoleucine catabolic pathway, tiglylglycine, 2-methyl-3-hydroxybutyrate, and 2-methylacetoacetate (*11*). This indicates that the interference of T2 deficiency with the ketolytic activity is more important than the interference with the ketone body synthesis.

The structures of the bacterial CT (bCT) from *Zoogloea ramigera* and the human CT (hCT) have been described (*13*, *14*). The kinetic properties of bCT (*15*) and hCT (*16*) have also been characterized. These tetrameric thiolases consist of four identical monomers, which are loosely associated as a dimer of dimers. Each monomer has the characteristic conserved structure of the thiolase superfamily fold (*2*). This thiolase fold can be subdivided into two halves, the N-terminal half and the C-terminal half, which have the same $\beta\alpha\beta\alpha\beta\alpha\beta\beta$ topology (*2*). The third component of the thiolase fold is the loop domain that protrudes out of the N-terminal half and consists of approximately 120 residues. This loop domain has a complex structure and multiple roles: it shapes the binding site of the CoA moiety of the substrate, it covers the active site cavity, and its tetramerization loop is an absolute requirement for the tetrameric assembly of the enzyme. The active site of thiolases is constructed on top of four loops, one from the N-terminal half (Nβ3−Nα3) and three from the C-terminal half (Cβ2−Cα2, Cβ3−Cα3, and Cβ4−Cβ5) (Figure 2) (*2*).

In the synthetic direction, the first step of the catalytic cycle is the acetylation of the catalytic cysteine by acetyl-CoA (*17*). Subsequently, CoA dissociates, and a second acetyl-CoA molecule binds in the active site followed by a Claisen condensation reaction in which acetoacetyl-CoA is formed (Figure 1A). In the degradative direction, these steps are reversed. First, the catalytic cysteine is acetylated by acetoacetyl-CoA, releasing acetyl-CoA, and the acetyl group coupled to the cysteine is then transferred to CoA, releasing a second molecule of acetyl-CoA. The key catalytic cysteine, which is covalently modified at the intermediate stage of the reaction cycle (Figure 1A), protrudes out of the Nβ3−Nα3 loop. The Cβ2−Cα2 loop, with the highly conserved NEAF sequence motif, stabilizes a conserved active site water molecule, hydrogen bonded to the asparagine side chain of this motif. The Cβ3−Cα3 loop provides the catalytic histidine and the Cβ4−Cβ5 hairpin loop the catalytic base, a cysteine, for the Claisen condensation reaction. Another key feature of the active site is the presence of two oxyanion holes. Oxyanion hole 1 is formed by the conserved active site water and the catalytic histidine; oxyanion hole 2 is formed by peptide NH groups of the Nβ3−Nα3 loop and the Cβ4−Cβ5 loop. These two oxyanion holes facilitate the catalysis by stabilizing a negative charge developing during the reaction cycle on the thioester oxygen of acetyl-CoA and the acetylated cysteine, respectively (*2*).

Here we describe the unliganded and liganded (with CoA and with K^+) structures of the human mitochondrial recombinant tetrameric thiolase, T2, and the structural differences with CT are discussed. The effects of potassium ions on the structure and on the steady state kinetic properties of T2 are also reported. In addition, we find, unexpectedly, that each

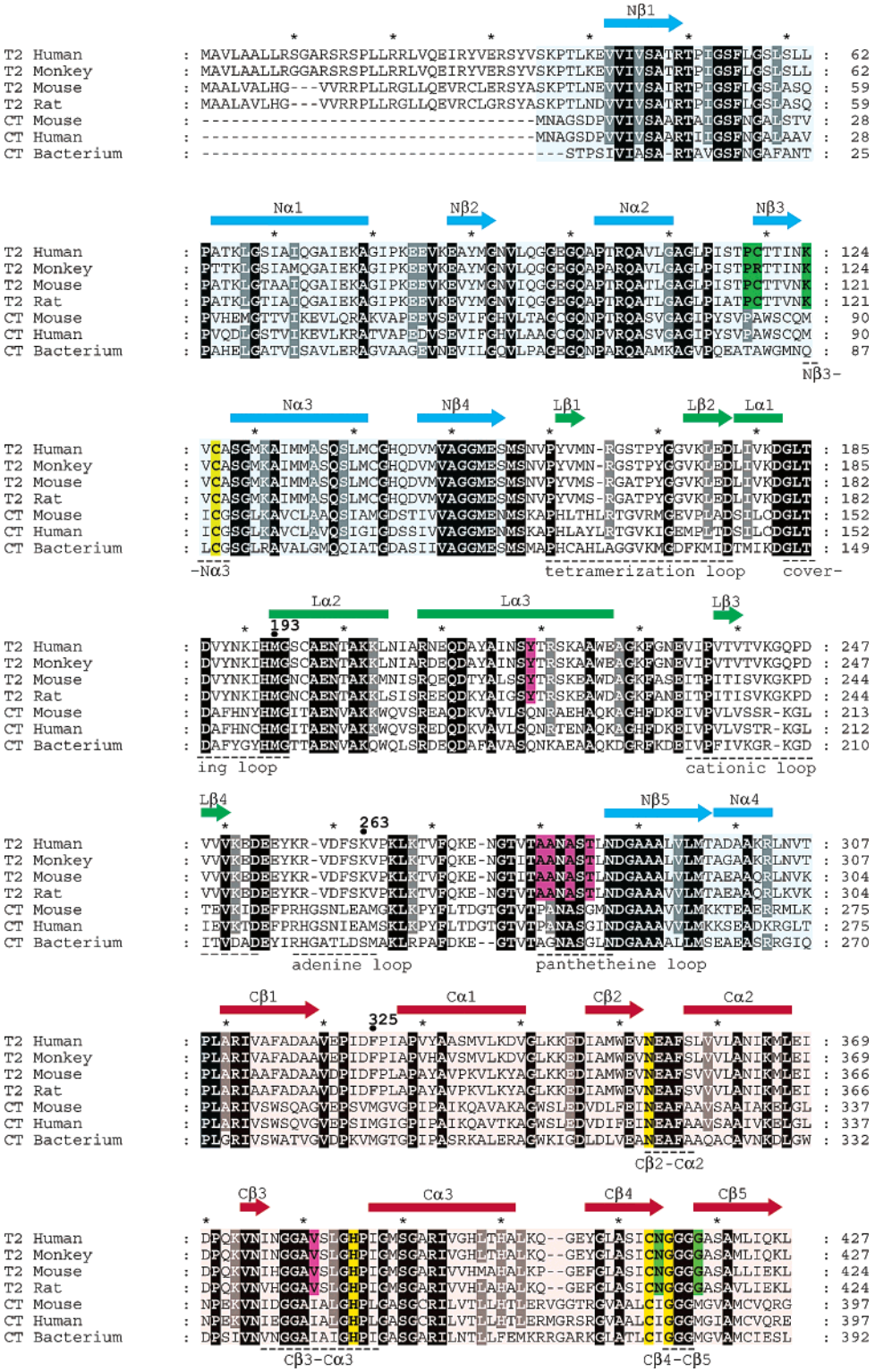

FIGURE 2: Sequence alignment of T2 (human, monkey, mouse, and rat) with CT [mouse, human, and bacterial (*Z. ramigera*)]. The secondary structure elements of human T2 have been identified by DSSP (*67*) and are shown above the sequences; bars for α-helices and arrows for *β*-strands. For clarity, asterisks denote every tenth residue in the human T2 sequence. The thiolase fold of the thiolase superfamily consists of three parts: the N-terminal half, the C-terminal half, and a loop domain. In the alignment, these are colored differently with the N-terminal half (Pro37−Ser155 and Asn287−Leu309 in human T2) colored blue, the C-terminal half (Ala310−Leu427 in human T2) colored red, and a loop domain (Met156−Leu286 in human T2) not colored. The secondary structure elements are colored blue, green, and red for the N-terminal half, the loop domain, and the C-terminal half, respectively. Residues conserved throughout the sequences are highlighted in black, and the others in a region with a high degree of sequence similarity are highlighted in dark gray (80−90%). Cys126, Asn353, His385, Cys413, and Gly415 participate in the thiolase reaction cycle and are highlighted in yellow. The residues with atoms which are coordinating the bound potassium ion are colored purple, and those residues in contact with the chloride ion are colored green. Met193 has a dual and fixed conformation in apoT2 and holoT2, respectively. Lys263 forms a salt bridge with the 3′-phosphate moiety of CoA. Phe325 is the putative interaction site for the 2-methyl group of the substrate. N*β*3−Nα3, C*β*2−Cα2, C*β*3−Cα3, and C*β*4−C*β*5 are the conserved catalytic loops of the catalytic site. The labeled loops of the loop domain (tetramerization loop, covering loop, cationic loop, adenine loop, and pantetheine loop) are described in more detail in the text.

subunit has a tightly bound chloride ion near the active site.

EXPERIMENTAL PROCEDURES

Construction of Plasmid pET3d::T2. Standard molecular biology methods described by Sambrook and co-workers (*18*) were applied to construct the *pET3d::T2* plasmid expressing human mitochondrial recombinant T2. Originally, the cDNA encoding human T2 was cloned from a hepatic cDNA library (*19*) after which the cDNA of interest was subcloned into the pCAGGS shuttle vector (*20*). The resulting plasmid was used as a template in the polymerase chain reactions (PCR), via which the used constructs were made. To maximize the chance for obtaining soluble protein and ultimately crystals, three variants of T2 were designed: with and without the mitochondrial targeting signal and having the same amount of residues at the N-terminus as bCT (Figure 2).

The coding regions for T2 were amplified by the PCR method using three kinds of forward and reverse primer pairs: (i) 5′-cacttcc ATG GCT GTG CTG GCG GCA CTT-3′ and 5′-catctggatcctca CTA CAG CTT CTG AAT TAG CAT GG-3′ (reverse primer), (ii) 5′-cacttcc atg GcA TCA AAA CCC ACT TTG AAG GGA G-3′ and the reverse primer, and (iii) 5′-cacttcc atg gCC ACT TTG AAG GAA GTG GTC ATA-5′ and the reverse primer. The lowercase sequences indicate mismatches to the T2 sequence, and underlined sequences are the introduced *Nco*I site at the 5′ end and the *Bam*HI site at the 3′ end of the PCR product. The three kinds of PCR products were isolated from an agarose gel and subcloned into the pMOS*Blue* vector. The nucleotide sequences of the inserted DNAs were verified. The introduced *Nco*I and *Bam*HI restriction endonuclease sites allowed the release of 1305, 1209, and 1200 bp inserts followed by subcloning into a similarly digested pET-3d expression vector. This yielded three kinds of plasmids that were different only at the 5′ end of their inserts; the plasmids were transformed in *Escherichia coli* BL21(DE3) pLysS cells for expression experiments. The 1305 bp insert, obtained with the first primer pair, encoded human recombinant precursor T2 of 427 amino acids, and the 1209 bp DNA fragment encoded a 394-residue mature enzyme without the N-terminal mitochondrial targeting signal (*19*). The third variant of the enzyme had three residues less than the mature T2.

Production, Purification, and Crystallization of Human Recombinant T2. E. coli BL21(DE3) pLysS cells transformed with the *pET3d::T2* plasmid were first cultured in 50 mL of Luria broth (LB) supplemented with 50 μg/mL carbenicillin and 34 μg/mL chloramphenicol overnight. For the production of recombinant T2, 10 mL of the overnight culture was used to inoculate 1 L of M9ZB medium containing the same amount of antibiotics as the LB. At an OD_{600} of approximately 0.4, the expression of the recombinant enzyme was induced by the addition of isopropyl β-D-thiogalactopyranoside (IPTG) to a final concentration of 0.4 mM. After incubation for an additional 3 h at 37 °C, the cells were harvested by centrifugation, washed with the buffer [120 mM NaCl, 16 mM potassium phosphate (pH 7.4), and 0.02% sodium azide], and stored at −70 °C. The longest and the shortest construct were only detected in the insoluble fraction. The recombinant T2 without the mitochondrial targeting signal and the N-terminal valine substituted with alanine (Val34Ala till Leu427), however, remained soluble when expressed in *E. coli*.

The recombinant T2 (V34A-L427) was purified to homogeneity using a three-step purification protocol: cation exchange chromatography, hydrophobic interaction chromatography, and gel filtration chromatography. A bacterial cell pellet (4.9 g wet weight) was resuspended in 100 mL of 30 mM 4-(2-hydroxyethyl)-1-piperazineethanesulfonic acid (HEPES), 30 mM NaCl, 1.5 mM NaN_3, and 5 mM dithiothreitol (DTT) (pH 6.6) (buffer A). The *E. coli* strain for producing recombinant T2 also expressed recombinant lysozyme to facilitate cell breakage. Cell lysis was further enhanced by adding 100 μg/mL lysozyme to the cell suspension. The viscosity of the solution was reduced by supplying 25 μg/mL DNase I, 25 μg/mL RNase A, and 5 mM $MgCl_2$. Ethylenediaminetetraacetic acid (EDTA) free protease inhibitor cocktail mixture (Roche Diagnostics GmbH) was also added to inhibit serine and cysteine proteases. The suspension was incubated at room temperature for 20 min. Cell debris from broken bacterial cells was collected by centrifugation (30000*g* for 45 min at 4 °C), and the supernatant was applied to a cation exchange CM Sepharose column (40 mL) equilibrated with buffer A. Some of the bound proteins, including recombinant T2, were eluted with a linear gradient from 30 to 240 mM NaCl for 10 column volumes at a flow rate of 1 mL/min. The fractions containing recombinant T2 were pooled, dialyzed against 50 mM sodium phosphate, 1.5 M $(NH_4)_2SO_4$, 1 mM NaN_3, 1 mM DTT, and 1 mM EDTA (pH 6.8) (buffer B), and applied to hydrophobic interaction Resource ISO column (1 mL) equilibrated with the same buffer. The column was washed with buffer B containing 1.2 M $(NH_4)_2SO_4$ and eluted with a 20 mL linear gradient from 1.2 to 0.975 M $(NH_4)_2SO_4$. Fractions (1 mL) were collected, and those containing thiolase activities (see Thiolase Assays) were pooled and concentrated to 2.5 mL on the Millipore concentrator. A 300 μL aliquot of the concentrated sample was applied to a size exclusion chromatography Superdex 200 HR 10/30 column that had been equilibrated with 30 mM HEPES, 1 mM EDTA, 1 mM NaN_3, 5 mM DTT, and 150 mM NaCl (pH 6.8) (buffer C). The column was eluted with the same buffer, and 300 μL fractions were collected at a flow rate of 250 μL/min and assayed for thiolase activity. Active fractions were pooled and concentrated to 8 mg/mL. The protein concentrations were measured with the Bio-Rad protein assay reagent using bovine serum albumin (BSA) as the standard. The purified enzyme exhibited cross-reactivity with a primary antibody, the rabbit anti-T2 antibody (*21*) (data not shown). Mass spectrometric analysis, SDS−polyacrylamide gel electrophoresis, activity measurements, and immunoblot analysis (*21*) were performed on the purified recombinant enzyme to confirm the purity and identity of the human recombinant T2. Aliquots (50 μL) of the concentrated enzyme, dissolved in buffer C, were rapidly frozen in liquid nitrogen by the PCR-tube method (*22*) and stored at −70 °C until they were used.

Prior to the crystallization experiments, the T2 stock solution was quickly thawed and diluted to 5 mg/mL with H_2O. Initial crystallization screening was conducted by the method described by Jankarik and Kim (*23*, *24*). Crystals suitable for data collection (0.25 mm × 0.15 mm × 0.05 mm) were obtained in 10 days by the hanging drop

vapor diffusion method at 4 °C by mixing 1.5 μL of protein solution with 1.5 μL of reservoir solution [100 mM 2-(*N*-morpholino)ethanesulfonic acid (MES) (pH 6.5) and 17−19% (w/v) polyethylene glycol 5000 monomethyl ether (PEG-5000-MME)]. Crystals of the same type, but containing T2 complexed with CoA, were obtained by cocrystallization of recombinant T2 with 2 mM CoA using otherwise the same conditions described above.

Production and Purification of Human Heart Recombinant Short Chain L-3-Hydroxyacyl-CoA Dehydrogenase. For the production of human heart recombinant short chain L-3-hydroxyacyl-CoA dehydrogenase, the plasmid, *rSCHADH6* (*25*), was transformed into the *E. coli* BL21(DE3) pLysS strain and cultured as described above for T2, except for the antibiotics, which where in this case 30 μg/mL kanamycin and 34 μg/mL chloramphenicol, and the cells were inducted at 30 °C for 4 h with 0.4 mM IPTG. After the harvesting and freezing steps, the cells were resuspended in 50 mM sodium phosphate, 50 mM NaCl (pH 8.0) buffer and the cells were lysed as described above. Protein purification was performed according to the method of Barycki and co-workers (*25*). The purified protein was stored at 4 °C, and its activity was assayed by following the degradation of acetoacetyl-CoA by applying the Mg^{2+} method (*6*). The reaction mixture consisted of 50 mM Tris-HCl (pH 8.1), 20 mM $MgCl_2$, 60 μM acetoacetyl-CoA, and 0.2 mM nicotinamide adenine dinucleotide (NADH). The reaction was started by adding an appropriate amount of enzyme, and the disappearance of the Mg^{2+} complex of acetoacetyl-CoA was followed at 303 nm and 25 °C for 5 min. One unit of L-3-hydroxyacyl-CoA dehydrogenase was determined to be the amount of enzyme that catalyzes the conversion of 1 μmol of acetoacetyl-CoA into L-3-hydroxybutanoyl-CoA.

Synthesis of 2-Methylacetoacetyl-CoA. 2-Methylacetoacetyl-CoA was synthesized by using the ethyl ester of 2-methylacetoacetate as a starting material, which was first hydrolyzed with NaOH and then washed with petrol ether to remove the ethyl ester part of the starting material. The remaining solution was acidified with HCl and extracted with ether, after which the ether layer was dried with $MgSO_4$. Freshly distilled thionyl chloride was added slowly into the ether solution of 2-methylacetoacetic acid and refluxed for 2 h. Excess $SOCl_2$ and ether were eliminated by evaporation to dryness (*26*). The prepared 2-methylacetoacetoyl chloride was used to acylate CoA (trilithium salt) at pH 8.5. Approximately 25 mg of CoA was dissolved in 2 mL of 0.4 M $KHCO_3$ to which the acyl chloride was added in small aliquots. The disappearance of free CoA was followed with an Ellman's test (*27*). When all the free CoA was consumed, the solution was acidified to pH 1 with 4 M HCl and extracted with diethyl ether to remove any free 2-methylacetoacetic acid (*8*). The solution was evaporated to dryness, dissolved in H_2O, and purified with the Silica RP C18 column (32−63 μm, 60 Å). Fractions were analyzed via thin layer chromatography. The fractions containing 2-methylacetoacetyl-CoA were pooled, evaporated to dryness, and preserved in −20 °C. When the product was identified via MALDI-TOF mass spectrometry (Voyager-DE STR Biospectrometry Workstation, Applied Biosystgems), one main peak (*m*/*z* 866.24) was found corresponding to 2-methylacetoacetoyl-CoA (M_w = 865.5 Da) (data not shown).

Thiolase Assays. The thiolytic assay of the breakdown of acetoacetyl-CoA by T2 was performed using the Mg^{2+} method as described previously (*6*) with a few modifications. The standard reaction mixture contained 50 mM Tris-HCl (pH 8.1), 20 mM $MgCl_2$, 60 μM CoA, 10 μM acetoacetyl-CoA, and either 40 mM KCl or 40 mM NaCl in a final volume of 0.3 mL. The change in absorption at 303 nm was followed for 10 min after addition of either 0.1 μg of T2 for the reaction mixture in the presence of KCl or 0.3 μg in the presence of NaCl. The temperature was set to 25 °C. In the determinations of K_m and V_{max} for acetoacetyl-CoA, the acetoacetyl-CoA concentration was varied in the range of 0.5−30 μM, and for the determination of the K_m of CoA, the CoA concentration was varied between 20 and 900 μM.

To determine the effect of potassium in the assay, the enzyme activity was measured by the Mg^{2+} method with different concentrations of K^+ and Na^+ ions, in such a way that the total concentration of salt was constant (120 mM). Salt concentrations were 0, 10, 20, 40, 60, 80, 100, and 120 mM for KCl, whereas NaCl concentrations were 120, 110, 100, 80, 60, 40, 20, and 0 mM.

K_m and V_{max} for the 2-methylacetoacetyl-CoA thiolytic cleavage reaction with T2 were determined by following the formation of new thioester bonds at 232 nm (*28*) and 25 °C. The reaction mixture contained 50 mM Tris-HCl (pH 8.1), 60 μM CoA, and either 40 mM NaCl or 40 mM KCl in a final volume of 0.3 mL. The concentration of 2-methylacetoacetyl-CoA was varied between 0.5 and 60 μM. The reaction was started by adding the enzyme, 25 ng for the KCl reactions and 100 ng for the NaCl reactions.

In the synthetic direction, from acetyl-CoA to acetoacetyl-CoA, the activity of T2 was measured by the assay described by Thompson and co-workers (*29*) with minor modifications. The reaction was started by adding 1 μg of T2 to the reaction mixture in a total volume of 0.3 mL containing 50 mM Tris-HCl (pH 7.4), either 40 mM KCl or 40 mM NaCl, 0.2 mM NADH, 1 unit of L-3-hydroxyacyl-CoA dehydrogenase, 0.5 mM DTT, and 0.1−2 mM acetyl-CoA. The rate of disappearance of NADH was followed at 340 nm. The assay was carried out at 30 °C.

All kinetic assays were conducted with a PowerWaveX microplate spectrophotometer. The changes in absorbance were measured immediately after the mixing phase, and the linear parts of these absorbance changes covering at least the first 3 min after the mixing were used for the rate calculations. The rates were corrected for the controls to which no enzyme was added. The concentrations of CoA and its derivatives were determined by using the Ellman's test (*27*); the CoA derivatives were first hydrolyzed by hydroxylamine, after which the Ellman's test was used for measuring the concentration of CoA.

The products of the thiolytic cleavage reaction of 2-methylacetoacetyl-CoA catalyzed by T2 were identified by mass spectrometry. A sample of the assay mixture was combined with 2,5-dihydroxybenzoic acid (50:50) and analyzed by the laser ionization method with a MALDI-TOF (Voyager-DE STR Biospectometry Workstation, Applied Biosystems) instrument. The samples were taken from a thiolytic assay mixture (see above) consisting of 60 μM 2-methylacetoacetyl-CoA, 40 mM KCl, 30 μM CoA, and either without T2 or with 250 ng of T2, after allowing equilibration for 4 min.

Table 1: Data Collection and Refinement Statistics

	apoT2 (PDB entry 2IB7)	apoT2+KCl (PDB entry 2IB8)	apoT2+KCl(ano) (PDB entry 2IB9)	T2+CoA (PDB entry 2IBU)	T2+CoA+KCl (PDB entry 2IBW)	T2+CoA+KNO_3 (PDB entry 2IBY)
			Data Collection			
space group	$P2_1$	$P2_1$	$P2_1$	$P2_1$	$P2_1$	$P2_1$
unit cell parameters						
a (Å)	75.26	75.65	75.75	75.25	76.14	75.35
b (Å)	106.49	107.28	107.44	106.57	107.58	106.75
c (Å)	101.73	102.21	102.33	101.50	101.95	101.66
β (deg)	102.95	103.07	103.06	102.90	102.89	103.06
temperature (K)	100	100	100	100	100	100
wavelength (Å)	0.8125	1.1410	1.4022	0.8115	1.1410	1.0722
resolution (Å)	73−2.05 (2.16−2.05)	47−1.85 (1.95−1.85)	74−2.05 (2.15−2.05)	20−1.90 (2.00−1.90)	48−1.90 (2.00−1.90)	73−1.85 (1.95−1.85)
R_{merge} (%)	7.8 (30.0)	6.1 (30.1)	7.3 (35.7)	6.8 (34.7)	8.3 (29.4)	6.9 (32.4)
completeness (%)	99.9 (99.9)	99.9 (100)	99.9 (99.9)	99.9 (100)	99.9 (99.9)	99.9 (100)
$I/\sigma I$	14.8 (5.2)	16.9 (4.6)	16.3 (3.9)	16.0 (4.3)	12.7 (4.8)	13.72 (4.6)
no. of unique reflections	97946 (14142)	135257 (19653)	99949 (13221)	122616 (17454)	125843 (17859)	133365 (19414)
redundancy	4.3 (4.2)	4.2 (4.1)	4.1 (4.1)	4.3 (4.2)	4.2 (4.1)	4.1 (4.1)
mosaicity (deg)	0.2	0.5	0.4	0.2	0.3	0.2
B-factor from Wilson plot ($Å^2$)	25	24	27	25	23	26
			Refinement Statistics			
resolution (Å)	73−2.05	47−1.85	74−2.05	20−1.90	48−1.90	73−1.85
total no. of reflections	97945	135259	99951	122615	125843	133365
no. of reflections in the working set	93047	128496	94953	116484	119551	126697
R_{factor} (%) for the working set	15.7	16.2	15.6	16.6	15.3	16.4
no. of reflections in the test set	4898	6763	4998	6131	6292	6668
R_{free} (%) for the test set	19.8	20.5	19.9	19.8	19.5	20.3
no. of protein atoms (A,B,C,D)	11567	11623	11634	11563	11635	11625
no. of water atoms	904	1033	938	1171	1100	1162
no. of CoA atoms				192	192	192
no. of potassium ions		4	4		4	4
no. of chloride ions	4	4	4	4	4	4
no. of glycerol atoms	30	30	30	6	6	12
no. of MES atoms	48	48	48		12	12
			Geometry Statistics			
rmsd for bond distances (Å)	0.012	0.013	0.012	0.011	0.012	0.011
rmsd for bond angles (deg)	1.3	1.3	1.3	1.3	1.3	1.3
rmsd for *B*						
main chain-bonded atoms ($Å^2$)	1.5	1.4	1.3	1.4	1.3	1.3
side chain-bonded atoms ($Å^2$)	1.6	1.7	1.5	1.6	1.5	1.6
main chain angle ($Å^2$)	2.1	2.0	2.0	2.0	1.9	2.0
side chain angle ($Å^2$)	2.2	2.3	2.1	2.2	2.2	2.2
average *B*						
main chain atoms ($Å^2$)	22.1	22.4	30.2	24.3	17.5	23.3
side chain atoms ($Å^2$)	24.1	24.5	32.3	26.3	19.5	25.5
water molecules ($Å^2$)	26.9	30.8	37.1	33.3	27.5	33.4
CoA atoms ($Å^2$)				49.1	39.6	43.5
potassium atoms ($Å^2$)		20.5	25.8		14.5	20.7
chloride atoms ($Å^2$)	18.0	18.3	27.5	19.3	15.4	48.9
glycerol atoms ($Å^2$)	44.5	42.7	55.2	31.1	43.2	37.4
MES atoms ($Å^2$)	64.6	71.2	83.1		65.3	76.1
Ramachandran plot						
most favored region (%)	93.1	93.5	93.0	93.0	93.3	93.4
additionally allowed regions (%)	6.6	6.2	6.7	6.7	6.4	6.3
generously allowed regions (%)	0.3	0.3	0.3	0.3	0.3	0.3
disallowed regions (%)	0	0	0	0	0	0

Data Collection and Processing. The first data sets were collected from an apo crystal (apoT2) and from a CoA-cocrystallized crystal (T2+CoA) (Table 1). Subsequently, crystallographic binding studies with and without potassium ions in the soaking solutions were initiated. Altogether, four more data sets were collected from the apo and CoA-

cocrystallized crystals using the following combinations (Table 1): apoT2 crystal soaked with 150 mM KCl (apoT2+KCl) as well as T2+CoA crystal soaked in the presence of either 150 mM KCl (T2+CoA+KCl) or 150 mM KNO_3 (T2+CoA+KNO_3). Additionally, the apoT2+KCl crystal was used to collect data at a higher wavelength (λ = 1.4022 Å) to obtain a better anomalous signal from the bound potassium and chloride ions [apoT2+KCl(ano)] (Table 1). All data sets were collected at cryogenic temperatures. In the case of binding studies, the crystals were first soaked in a reservoir solution, supplemented with the appropriate ligands at room temperature for 2 h after which the crystals were soaked briefly (2−3 min) in the cryo solution, at room temperature. The cryo solution included the relevant binding molecules, as well as 17.5% glycerol. After the cryo soak, the crystals were flash-frozen in liquid nitrogen. All the X-ray data were collected on a CCD detector at various beamlines at the European Synchrotron Radiation Facility (ESRF, Grenoble, France), MAX-lab (Lund, Sweden), and Deutsches Elektronen-Synchrotron (DESY, Hamburg, Germany). Images were processed and the intensities scaled and merged using the *XDS* program package (*30*, *31*). The data collection and processing statistics are listed in detail in Table 1. The recombinant T2 crystals belonged to monoclinic space group $P2_1$. For one tetramer per asymmetric unit, the Matthew's coefficient values (*32*) varied between 2.4 and 2.5 Å^3/Da which indicates a solvent content of 49−50%.

Structure Determination, Model Building, and Refinement. Molecular replacement calculations using hCT (PDB entry 1WL4) as a model were performed with *MOLREP* (*33*) of the *CCP4* program suite. For the molecular replacement calculations, the T2+CoA data set (Table 1) was used. The hCT model was a single monomer of the tetrameric enzyme. Since the Matthew's equation indicated that the T2 crystal contains four identical monomers per asymmetric unit, four rounds of rotational and translational searches were performed to identify the T2 tetramer. Molecular replacement gave one good solution with a correlation coefficient of 40.1% (R = 48.2%). This solution was subjected to rigid body refinement, simulated annealing, and *B*-factor refinement with *CNS* (*34*). Of the diffraction data, 5% was used for cross validation. The *R*-factor of the model dropped to 41.7% (R_{free} = 44.9%) during this refinement, and the resulting model was used in the side chain docking step of *WARPNTRACE* (*35*) using the human T2 sequence. After the second round of refinement (including simulated annealing), the *R*-factor decreased to 31.7% (R_{free} = 35.4%). This structure was then used as a starting model in the subsequent refinement and model building steps with *REFMAC5* (*36*) and *O* (*37*), respectively.

The initial models of the other structures (Table 1) were obtained by rigid body refinement using only the protein part of the finalized T2+CoA structure as a starting model, and simulated annealing with *CNS* followed by refinement with *REFMAC5*. Water molecules were picked by using *ARP-WARP* (*35*) in the solvent building mode. Only those waters were accepted that were within reasonable distance of hydrogen bonding partners and had a difference density of $>3\sigma$. CoA, chloride, and/or potassium ions identified in $F_o - F_c$ electron density maps at this stage were included in the refinement cycles, as well. Throughout the refinement, the quality of the models was checked by the structure validation programs *PROCHECK* (*38*) and *WHAT IF* (*39*). The refinement and geometry statistics of all the structures in this study are presented in Table 1.

Identification of the Ion Binding Sites. The electron density maps of the apoT2 and T2+CoA crystals (Table 1), soaked in mother liquor supplemented with 150 mM KCl, revealed one extra ion binding site per subunit near the adenine moiety of the CoA. When refined as a K^+ ion, the *B*-factors reached reasonable values and were in the same range that was obtained for the surrounding protein atoms. By using KNO_3 instead of KCl in the soaking experiment with a T2+CoA crystal resulting in T2+CoA+KNO_3 structure (Table 1), both the peak heights and locations in the $F_o - F_c$ map were in the same range and place, respectively, as those obtained for K^+ with T2+CoA+KCl and T2+KCl crystals. Thus, the identified K^+ binding site was confirmed, and the binding of a chloride ion at this site was ruled out. The corresponding site in the apoT2 and T2+CoA structures was occupied by an atom with the properties of an ordered water molecule. The peak heights of the potassium ions in the $2F_o - F_c$ electron density maps of the apoT2+KCl, T2+CoA+KCl, and T2+CoA+KNO_3 structures were as high as $\sim 10\sigma$. In the maps, there was for each subunit a second ionic site of approximately the same peak height. This site was also occupied in the apoT2 and T2+CoA structures, for which the crystals were not treated with 150 mM KCl or 150 mM KNO_3. Apparently, this ion is tightly bound and is copurified. As the electron density peak height at this site was very similar to that of the identified K^+ site, this ion could be a second potassium ion or alternatively a chloride ion, each of which has the same amount of electrons. The second site is at the interface of the tight dimer and also near the Cβ4−Cβ5 and Nβ3−Nα3 active site loops. Both the potassium and the chloride ion have a relatively large, but similar, ionic radius, and the protein geometry at this second site does not uniquely exclude either a potassium or a chloride ion. Therefore, the peak heights of the anomalous Bijvoet difference map of the apoT2+KCl(ano) data set (Table 1) were analyzed. Different peak heights are expected as the f'' values for potassium and chlorine are substantially different. At the chosen wavelength of 1.4022 Å (λ), the f'' of K^+ equals 0.9 electron and the f'' of Cl^- 0.5 electron (*40*). In the obtained anomalous difference maps, the peak heights of the site near the residues at the adenine of the CoA binding site were in each monomer substantially higher than the peak heights of the ionic site near the Cβ4−Cβ5 loop. This rules out the possibility that the two ions are the same, and it can be concluded that a chloride ion is bound near the Cβ4−Cβ5 and Nβ3−Nα3 loops at the dimer interface. The peak heights in the anomalous difference maps of the lowest *B*-factor potassium ions are at 7.3σ, whereas the peak heights of the chloride ions with corresponding *B*-factors are at 4.1σ.

Structure Analysis. The final structures have been analyzed with *PROCHECK* (*38*), *WHATIF* (*39*), and *O* (*37*) and compared with the structures of the CoA-liganded structure of hCT (PDB entry 1WL4) and the acetylated bCT complexed with acetyl-CoA (PDB entry 1DM3). The structures have been superimposed using the LSQ option of *O*. For the active site superposition, the 28 C_α atoms of the four catalytic loops, Nβ3−Nα3, Cβ2−Cα2, Cβ3−Cα3, and Cβ4−Cβ5 (*2*), were used. In the T2 numbering scheme, the catalytic residues are Cys126 of the Nβ3−Nα3 loop, Asn353

Table 2: Kinetic Parameters of T2[a]

substrate	40 mM KCl		40 mM NaCl	
	K_m (μM)	k_{cat} (s^{-1})	K_m (μM)	k_{cat} (s^{-1})
acetoacetyl-CoA[b]	4 ± 0.6	21 ± 1	8 ± 2	7.4 ± 0.2
CoA[c]	20 ± 2	18 ± 2	66 ± 14	7 ± 1
2-methylacetoacetyl-CoA[b]	8 ± 1	61 ± 6	8 ± 1	14 ± 3
acetyl-CoA	508 ± 127	3.5 ± 0.7	>1000[d]	nd[d]

[a] All values are the average of multiple, independent measurements. [b] In the presence of 60 μM CoA. [c] In the presence of 10 μM acetoacetyl-CoA. [d] Reliable values could not be measured.

of the Cβ2−Cα2 loop, His385 of the Cβ3−Cα3 loop, and Cys413 of the Cβ4−Cβ5 loop. The model of 2-methylacetoacetyl-CoA was made with the Dundee PRODRG2 server (*41*). The van der Waals contacts between the 2-methylacetoacetyl-CoA and the protein were optimized with *REFMAC5* and checked manually. The figures have been made with *PyMOL* (*42*). The reference structure is subunit B of the T2+CoA+KCl structure (Table 1), unless otherwise stated.

RESULTS AND DISCUSSION

Kinetic Data. The steady state kinetic parameters of recombinant T2 were determined for both the thiolytic and synthetic reaction. The dependence of the T2 thiolytic activity on the presence of potassium ions was assayed by varying the concentration of potassium from 0 to 120 mM while keeping the ionic strength the same (see Experimental Procedures). It was found that T2 gained full activity when the concentration of KCl reached 40 mM, and the activity remained constant thereafter. Subsequently, the steady state kinetic parameters were determined at either 40 mM KCl or 40 mM NaCl, as summarized in Table 2. The k_{cat} values are approximately 3 times higher in the presence of 40 mM KCl, for the degradation of both acetoacetyl-CoA and 2-methylacetoacetyl-CoA. When the thiolytic cleavage is considered, it is seen that in the presence of potassium ions the K_m values of acetoacetyl-CoA and CoA are decreased, but for 2-methylacetoacetyl-CoA, the K_m is not affected. The very high affinity of T2 for acetoacetyl-CoA [$K_m = 4$ μM (this study)] and the weaker affinity for CoA [$K_m = 20$ μM (this study)] were also found by Middleton for rat T2 (*7*). The k_{cat}/K_m values are approximately 6 times higher in the presence of 40 mM KCl for the degradation of both acetoacetyl-CoA and 2-methylacetoacetyl-CoA. The k_{cat} values for the thiolytic degradation of acetoacetyl-CoA are 10 times lower than those found for CT (*14*, *16*, *43*). For the synthetic reaction, we observed that the K_m for the substrate becomes so high in the absence of potassium ion that it becomes impossible to measure reliably the K_m and the turnover number (Table 2).

The high degrees of similarity within the thiolase family of enzymes (*2*) suggest that T2 and CT will have a very similar reaction mechanism, indicating that in the degradation of 2-methylacetoacetyl-CoA in the presence of CoA the products will be propionyl-CoA and acetyl-CoA. Mass spectroscopy analyses indeed show that when 2-methylacetoacetyl-CoA and CoA are equilibrated with T2 propionyl-CoA and acetyl-CoA are formed (Figure 3).

Overall Structure. The high-resolution limit of the six data sets in this study varies from 1.85 to 2.05 Å (Table 1). For each of the six structures, the space group is the same, with one tetramer (Figure 4A) per asymmetric unit. Each of the structures has been refined with good stereochemistry (Table 1), and continuous density is observed for the main chain from residue Pro37 to Leu427. However, in monomer D of all the structures and in monomer C of T2+CoA, T2+CoA+KCl, and T2+CoA+KNO_3 structures (Table 1), the N-terminal region is visible from Ser35 onward. In apoT2, apoT2+KCl, and apoT2+KCl(ano) structures (Table 1), on the other hand, the N-terminal region of monomer C is visible from Lys36 onward. The four independent subunits of the tetramer are essentially the same for each structure; the rmsd differences for the corresponding C_α atoms of superimposed subunits are approximately 0.4 Å. The structures have at least 93.0% of their residues in the most favored region as judged from the Ramachandran statistics (Table 1). None of the residues are in the disallowed region. Only one residue per each monomer in every structure is located in the generously allowed region; it concerns Val125 ($\phi = 49°$; $\psi = -133°$) in the Nβ3−Nα3 loop, just before the active site cysteine, Cys126. Similarly strained values for the corresponding residue in other thiolase structures have been reported previously (*14*).

The cores of the subunits consist of an $\alpha\beta\alpha\beta\alpha$ layered structure, in which the α-helices and β-sheets have arranged themselves in five subsequent layers (Figure 4B). The central layer is a helical bundle, consisting of the two active site helices, Nα3 and Cα3, of the N-terminal half and C-terminal half, respectively. These two helices are surrounded by β-sheets on both sides which, in turn, are covered again by helices which also face the bulk solvent. The structures show that, in human T2, the N-terminal half of the thiolase fold is formed by residues Pro37−Ser155 together with Asn287−Leu309 and the C-terminal half by residues Ala310−Leu427, whereas the loop domain is formed by residues Met156−Leu286 (Figure 2). The loop domain covers the tightly associated N-terminal and C-terminal halves of the subunit (Figure 4B), and it has two characteristic protruding loops: the tetramerization loop (Pro160−Asp177) and the cationic loop (Val232−Asp253) (Figure 2). The tetramerization loop and the cationic loop protrude not only out of the monomer (Figure 4B) but also out of the tight dimer (Figure 5). The tetramerization loop stabilizes the tetramer. The positively charged basic residues at the tip of the cationic loop point to the substrate binding site of the opposing dimer (Figure 4A).

The structure of T2 complexed with CoA, determined from a crystal cocrystallized with CoA (T2+CoA), shows that the binding of CoA does not induce structural changes, as the structures of apoT2 and T2+CoA are the same. Equal occupancy for the CoA molecules in each of the four active sites is observed, and the mode of binding of CoA is well-defined by the electron density maps.

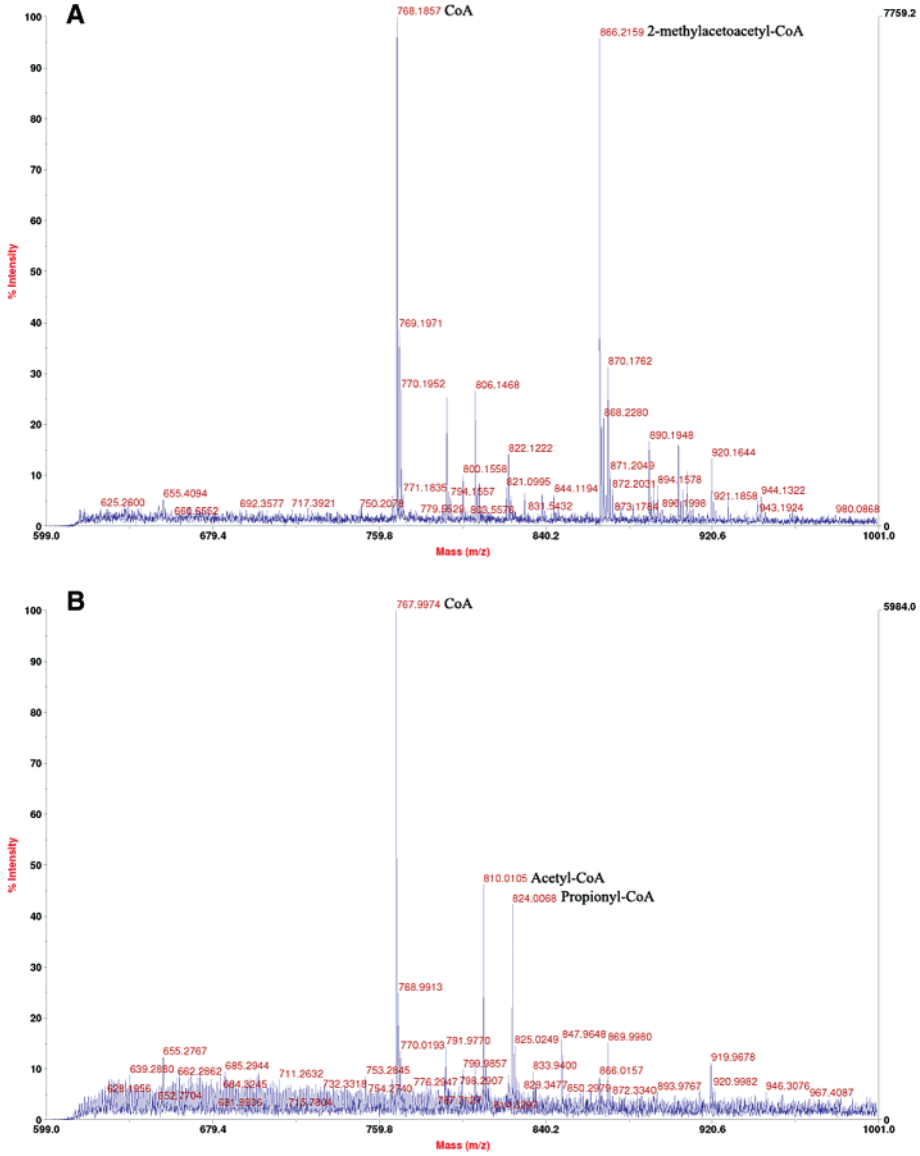

FIGURE 3: Mass spectrometric experiments on the thiolytic degradation of 2-methylacetoacetyl-CoA by T2. (A) Mass spectrum of the reaction assay mixture without T2. (B) Mass spectrum of the reaction assay mixture after the addition of T2, showing that 2-methylacetoacetyl-CoA is converted into acetyl-CoA and propionyl-CoA by T2.

The most significant differences between T2 and CT occur in the loop domain, such as in the precise structure of the region that shapes the adenine binding site (residues 256−269). In T2, this region is two residues shorter than in CT (Figure 2). With this arrangement, T2 accommodates the bound substrate more tightly. Other differences in the loop domain relate to the properties of the cationic loop and the tetramerization loop. The sequences of these loops also exhibit very little sequence conservation between T2s and CTs (Figure 2). The tetramerization loop is one residue shorter (Figure 2). The solvent-exposed cationic loop, which in T2 is one residue longer, is thought to play an important role in capturing the negatively charged substrate molecule in the active site of the opposing dimer (*14*). In T2, this loop is less positively charged since it has only one lysine, Lys243, instead of two lysines, as in CT. However, in T2, there are five additional lysines near the CoA binding pocket, Lys257, Lys263, Lys266, Lys268, and Lys273, whereas in CT, there are only four basic residues in this region. Lys257, Lys263, and Lys268 have been replaced with arginine, serine, and arginine, respectively, in CT.

Potassium Ion Binding Site. The potassium ion binding site is shaped by main chain and side chain atoms of residues of the loop domain and the catalytic Cβ3−Cα3 loop (Figures 2 and 6A). No such potassium ion site is observed in other known thiolase structures. The K^+ is within 2.7−3.1 Å of the four main chain oxygens of Ala280, Ala281, Ala283, and Val381 (Table 3). The two other oxygens coordinating the bound K^+ are the OH group of Tyr219 of the long and prominent helix of the loop domain (at 2.9 Å) and a water molecule (at 2.8 Å) (Figure 6A). Such a coordination by six oxygen atoms with an average distance of 2.8 Å is characteristic of a K^+ ion binding site (*44*). Additionally, the K^+ ion is in van der Waals contact, within 3.8 Å, with several carbon atoms of Ala281, Ala283, and Thr285. The potassium ion shapes the adenine binding pocket as two of its coordinating oxygen atoms, the OH group of Tyr219 as well as the coordinating water molecule, interact with the adenine moiety of CoA (Figure 6A). The binding of K^+ does not induce conformational changes in the loops shaping its binding site. However, from the *B*-factor plots (data not shown), it is evident that the presence of K^+ does

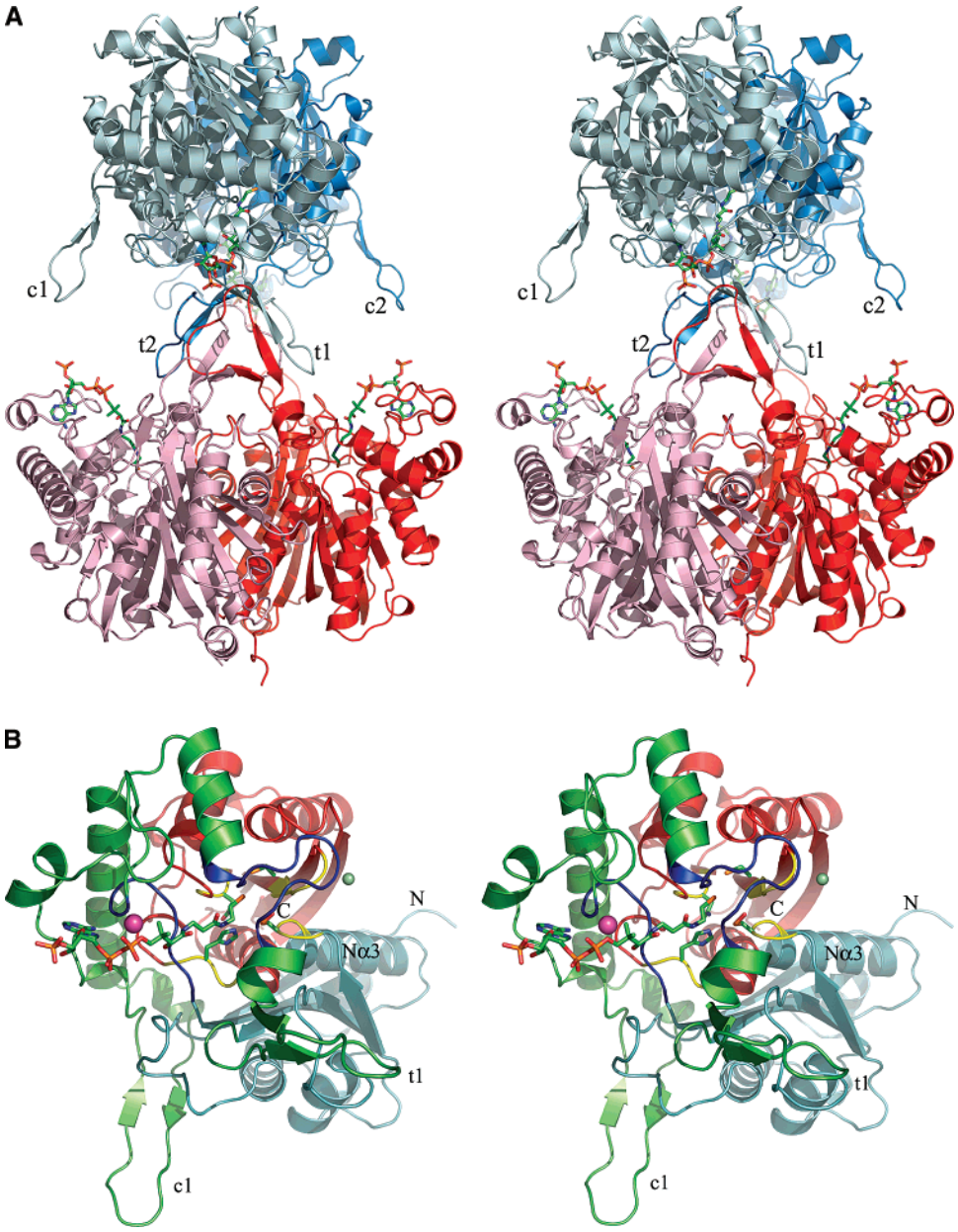

FIGURE 4: Overall structure of human T2. (A) Quaternary structure of the T2 homotetramer. The structure is drawn as ribbons, and the four monomers are colored differently. The bound substrate in every monomer is CoA which is shown as atom-colored skeletons. The protruding loop at the interdimer space is the cationic loop and labeled as c1 and c2 for monomer 1 and monomer 2, respectively. Additionally, the tetramerization loops of monomers 1 and 2 are labeled as t1 and t2, respectively. (B) Tertiary structure of the human T2 monomer. The core of the fold, consisting of the N-terminal (blue) and C-terminal (red) halves, has a $\alpha\beta\alpha\beta\alpha$-layered structure which is characteristic of the members of the thiolase superfamily. The two helices, Nα3 and Cα3, comprise the central helical bundle of the layered structure. The loop domain (green) provides the binding site for CoA. The color code for the N- and C-terminal halves as well as for the loop domain is the same as that used in Figure 2. Additionally, the four catalytic loops are colored yellow; the side chains of each of the four respective catalytic residues, Cys126, Asn353, His385, and Cys413, are also shown. The regions colored blue are the covering loop that covers the catalytic cavity and the pantetheine loop which interacts with the pantetheine part of the bound CoA. The potassium ion is shown as a magenta sphere and the chloride ion as a green sphere. N and C label the N-terminus and C-terminus, respectively. The labeling of the cationic and tetramerization loops is consistent with panel A.

rigidify the region of Thr279−Thr285, as well as the region adjacent to Val381 of the active site Cβ3−Cα3 loop, including His385, which is one of the catalytic residues. The residues Thr279−Thr285 are at the C-terminal end of the loop domain and are involved in binding the pantetheine moiety of the substrate. At present, K^+-activated enzymes are divided into two groups: type 1 and type 2 (*45*). In the type 1 subgroup, the K^+ ion acts as a cofactor, and it is needed to position the substrate properly in the active site of an enzyme; therefore, the presence of K^+ is required for the enzymatic activity. In type 2 enzymes, the K^+ is an allosteric factor. In this case, K^+ makes no direct contact with the substrate but affects the orientation of the active site residues. Type 2 enzymes are functional even without K^+. T2 is like the enzyme in the latter subgroup since K^+ is not directly interacting with the bound substrate and T2 is able to catalyze the reaction cycle in the absence of K^+. From the structures of this study, we can see that with respect to catalytic efficiency, the K^+ has a dual role. It rigidifies one of the active site loops and thereby stabilizes the catalytic

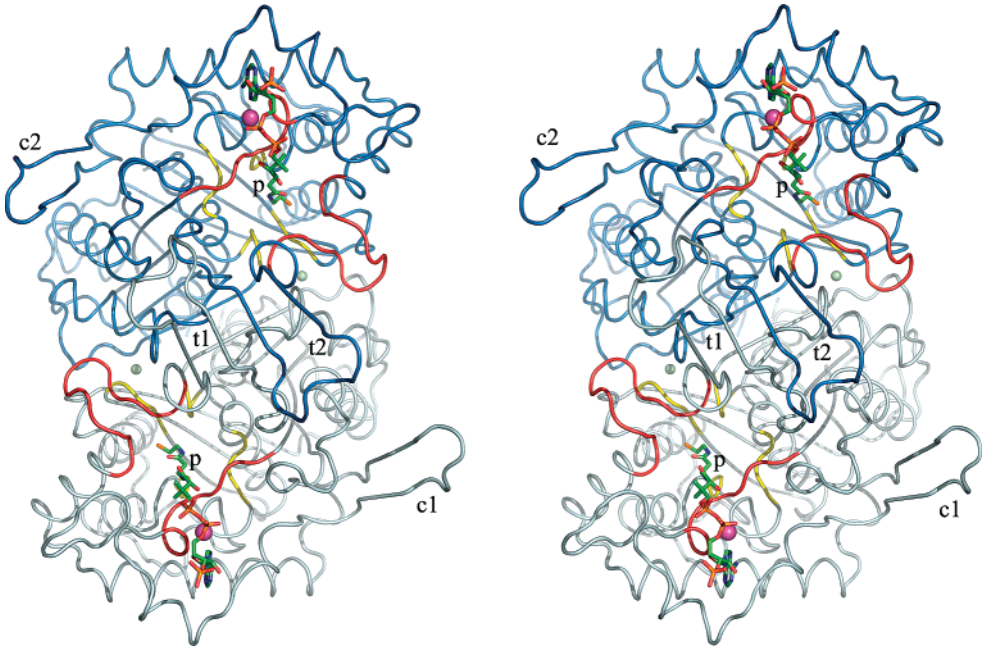

FIGURE 5: Human T2 dimer. The view is along the local twofold axis, looking down from the opposing dimer. The half-barrel of the tetramerization region, formed by the antiparallel β-strands of the tetramerization loops (t_1 and t_2) of both monomers of the dimer, is seen in the center of the structure. The protruding cationic loops of monomers 1 and 2 are labeled as c1 and c2, respectively. The catalytic loops are colored yellow, and the covering loop and the pantetheine loop are colored red. The pantetheine loop interacts with the bound substrate which is CoA. The potassium ion close to the adenine ring of CoA is shown as a magenta sphere. The two green spheres at the dimer interface are the chloride ions. The pantetheine part of CoA, near the catalytic cavity, is labeled p.

histidine, resulting in higher turnover numbers. In addition, the adenine of CoA interacts with the K^+ coordinating groups, and the presence of the bound K^+ increases the affinity of the substrates (Table 2).

T2 has weak affinity for potassium ions, as full activation is achieved when the potassium ion concentration increases from 0 to 40 mM. The K^+ concentration in the cytosol is approximately 150 mM, but studies indicate that the intramitochondrial K^+ concentration can vary from 15 to 150 mM (*46*−*50*). Also, various kinds of K^+ channels, including a K^+/H^+ antiporter, have been characterized in the mitochondrial inner membrane (*51*−*55*). These findings indicate that the concentration of K^+ in the mitochondrial matrix is regulated and can be different from the concentration in the cytosol. Moreover, it has been noted that the uptake of K^+ by the mitochondrial matrix is related to an increased rate of mitochondrial fatty acid β-oxidation and respiration (*56*−*58*). In this context, it is of interest to note that the mitochondrial pyruvate dehydrogenase complex which converts pyruvate from the glycolytic pathway into acetyl-CoA for the respiratory pathway is also dependent on K^+ (*59*, *60*), whereas if fatty acyl-CoA is the energy source, then acetyl-CoA is generated by the K^+-dependent T2. Apparently, higher potassium ion concentrations increase the catalytic efficiency of those enzymes that provide the substrate of the citric acid cycle, suggesting that the K^+ activation of these enzymes could be a regulatory mechanism *in vivo*.

Mode of Binding of CoA. The CoA molecule can be divided into a 3′-phosphate adenosine, pyrophosphate, and pantetheine moiety (Figure 1B). In T2, the bound CoA molecule has a characteristic bend at the pyrophosphate moiety causing its overall curved conformation (Figures 4 and 5). The ribose ring of the adenosine shows *C2′-endo* puckering, and the torsion angle of the glycosidic bond between the ribose and the purine base refers to the *anti* conformation. The structural differences in the loop domain correlate with small but significant differences in the mode of binding of the 3′-phosphate adenosine and pyrophosphate parts of CoA when T2 and CT are compared. In T2, the adenine ring itself is bound to a small cleft lined by side chains of Tyr219, Arg258, Val259, Asp260, Lys263, Val264, Leu267, Ala280, and Ala281. The stacking interaction of an arginine side chain with the adenine moiety, as seen in CT (*17*, *61*) structures, is absent in T2. Instead, main chain to adenine hydrogen bonds are observed with the Arg258, Val259, and Asp260 residues of the adenine loop (Figure 2). These interactions are very similar to the "ADA"−adenine interaction motif described by Denessiouk and Johnson (*62*). The corresponding interactions of this motif are as follows: O(Val259)−NA6(adenine) (3.6 Å), N(Asp260)−NA1(adenine) (3.3 Å), and O(Asp260)−CA2(adenine) (3.3 Å). There is one additional direct hydrogen bond between the adenine ring and the protein [OH(Tyr219)−NA6(adenine) (Figure 6A and Table 3)]. The 3′-phosphate attached to the ribose is part of a salt bridge (2.9 Å) with the positively charged NZ(Lys263). Lys263, which is also hydrogen bonded to the ribose hydroxyl groups, is not conserved among thiolases (Figure 2). The salt bridge between NZ(Lys263) and the 3′-phosphate moiety is the only salt bridge interaction between T2 and CoA.

The pantetheine part of CoA dives into a narrow and rigid tunnel. At the bottom of this tunnel is the active site, lined by the side chains of the four catalytic loops. This tunnel is shaped by two loops, which both are part of the loop domain: the covering loop (residues 179−194) and the pantetheine loop (residues 280−285) (Figure 2). These loops are highlighted in red in, for example, Figures 5 and 6B. The covering loop covers the active site and is at the

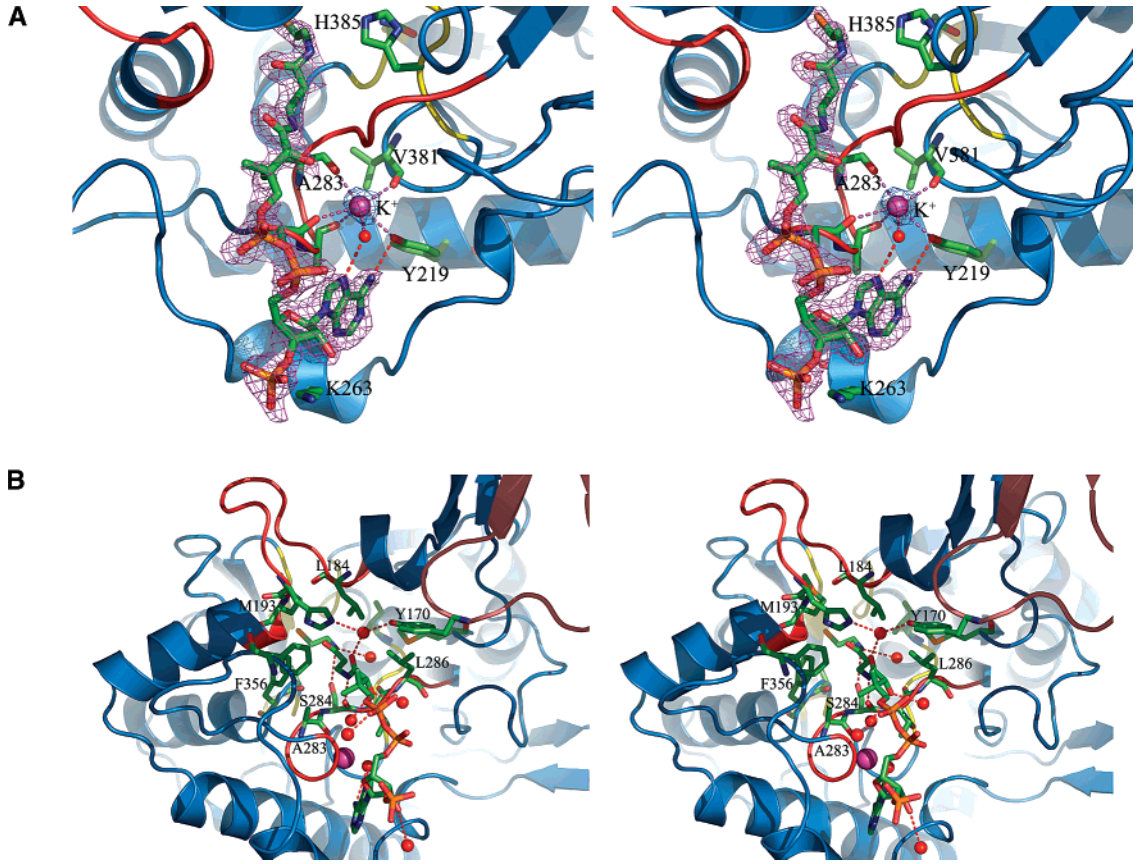

FIGURE 6: Mode of binding of the potassium ion and CoA. (A) Potassium ion binding site. The potassium ion is coordinated (magenta dashed lines) by a water molecule, the hydroxyl group of Tyr219, and the main chain oxygen atoms of Ala280, Ala281, Ala283, and Val381 (Table 3). The active site loops with the catalytic residues are colored yellow. The ligand, CoA, is shown as an atom-colored skeleton; two of the nitrogen atoms of the adenine moiety are hydrogen bonded (red dashed lines) to the members of the potassium coordination group. The figure also shows the $(F_o - F_c)\alpha_c$ omit map of the CoA region and the anomalous difference map at the potassium ion (K^+) site. These maps are contoured at 3σ and 2σ levels for CoA and K^+, respectively. The omit map was calculated after omit refinement, without including the relevant ligand in the refinement. (B) Pantetheine binding tunnel. Residues Ala283, Phe356, Met193, Leu184, Leu286, and Ser284 form the narrowest part of this tunnel. Tyr170 of the opposing dimer with a purple C_α trace is also labeled. Most of the hydrogen bonds (red dashed lines) between the CoA and T2 are via water molecules (red spheres) (Table 3).

beginning of the loop domain, just after the tetramerization loop. The pantetheine loop is at the very end of the loop domain. The depth of the tunnel, including the active site cavity, is approximately 17 Å. Even though the binding mode of the adenosine and pyrophosphate moieties is different from that of other thiolases, the conformation of the pantetheine moiety is conserved. The binding tunnel is in particular shaped by the side chains of Met156 (just before the tetramerization loop), Leu184, His192, and Met193 (of the covering loop), and Phe271, Ala283, Ser284, Thr285, and Leu286 (of the pantetheine loop). Additionally, Ala355 and Phe356 (of the active site Cβ2−Cα2 loop) and Ile387 (of the active site Cβ3−Cα3 loop) interact with the bound pantetheine. The pantetheine moiety engages in hydrophobic and polar interactions with the protein. As shown in Figure 6B, the narrowest part of the tunnel is formed by the side chains of Ala283, Phe356, Met193, Leu184, and Leu286. These residues form an almost complete ring of hydrophobic side chains; this ring is closed by the polar side chain of Ser284.

In addition to the five hydrogen bonds of the 3′-phosphate adenosine and pyrophosphate moieties (Table 3), there are two hydrogen bonds between the pantetheine group and the protein (Figure 6B and Table 3). The nitrogen, NP4 (Figure 1B), of the β-mercaptoethylamine moiety is hydrogen bonded to OG(Ser284), and NP8 has a hydrogen bond with the peptide oxygen of the same serine (Figure 6B). The OP5 atom is not hydrogen bonded to any polar atom. Moreover, there are altogether eight water-mediated hydrogen bonds to the protein, as listed in Table 3. These waters are also present in the apo structure. Three of these water molecules reside in the interior of the tunnel: one water is in contact with NP4, and two other water molecules are hydrogen bonded to the hydroxyl group (OPA) (Figure 1B) of the pantetheine. A fourth water molecule is part of an interesting interaction site seen at the entrance of the tunnel (Figure 6B). The site of the fourth water molecule is partly shaped by Tyr170 of the opposing dimer. The side chain of this tyrosine, protruding out of the tip of its tetramerization loop, is hydrogen bonded via this water molecule to OP9 of the pantetheine moiety, suggesting cooperation of the opposing dimers in substrate binding. Numerous van der Waals contacts between CoA and hydrophobic side chains of T2 supplement the listed polar interactions.

Chloride Ion Binding Site. The chloride ion is bound tightly, because it is copurified. It is coordinated by three oxygen atoms, two from water molecules and O(Cys119) of the neighboring subunit of the tight dimer (Table 3 and Figure 7). Other atoms from the same neighboring subunit involved in the coordination of this ion are N(Cys119) and

Table 3: Contact Distances for the K^+ Ion, the Cl^- Ion, and CoA

ligand	atom	distance (Å)[b]
K^+	OH(Tyr219)	2.9
K^+	O(Ala280)	3.1
K^+	O(Ala281)	2.8
K^+	O(Ala283)	2.7
K^+	O(Val381)	2.8
K^+	O(Wat209)	2.8
Cl^-	CE(Lys124)	3.9
Cl^-	ND2(Asn414)	3.5
Cl^-	CA(Gly418)	3.8
Cl^-	CA(Pro118)[a]	3.9
Cl^-	N(Cys119)[a]	3.4
Cl^-	O(Cys119)[a]	3.9
Cl^-	O(Wat58)	3.1
Cl^-	O(Wat220)	3.1
NA6 of CoA	OH(Tyr219)	2.9
NA1 of CoA	N(Asp260)	3.3
OR3 of CoA	NZ(Lys263)	2.9
OA9 of CoA	NZ(Lys263)	2.9
OR2 of CoA	NZ(Lys263)	3.0
NP8 of CoA	O(Ser284)	3.0
NP4 of CoA	OG(Ser284)	3.4
NP4 of CoA	O(Wat48)	3.4
OP9 of CoA	O(Wat330)	2.8
OPA of CoA	O(Wat216)	3.0
OPA of CoA	O(Wat116)	3.1
NA7 of CoA	O(Wat209)	2.9
NA6 of CoA	O(Wat209)	3.4
OA4 of CoA	O(Wat544)	2.6
OR2 of CoA	O(Wat1005)	3.4

[a] Atom of a neighboring subunit. [b] The cutoff values have been 3.5, 4.0, and 3.5 Å for K^+, Cl^-, and CoA, respectively. For CoA, only hydrogen bonding interactions are listed.

CA(Pro118). Otherwise, the ion is surrounded by atoms ND2(Asn414) and CA(Gly418) of the Cβ4−Cβ5 catalytic loop and CE(Lys124) of the other catalytic Nβ3−Nα3 loop (Table 3 and Figures 2 and 7). The closest atoms are the two water molecules, and the contact distance of 3.1 Å for these atoms is in good agreement with the analysis of the hydrogen bonding interactions of chloride ions (*63*, *64*). The contact distances to N(Cys119) (3.4 Å) and ND2(Asn414) (3.5 Å) also involve hydrogen bonds, whereas the other listed neighboring atoms are van der Waals contacts. In addition, the closest charged group is the positively charged NZ-(Lys124) atom at 4.2 Å. It is interesting to notice that one of the coordinating residues, Asn414, is between the catalytic base (Cys413) and Gly415 of oxyanion hole 2. Moreover, the other coordinating water molecule is hydrogen bonded to ND2(Asn414) and O(Gly415). The geometry of Gly415 is important as N(Gly415) is part of oxyanion hole 2. Clearly, the interactions of the bound chloride ion are important as it stabilizes the structures of two of the four active site loops.

The position of the chloride superimposes exactly on the sulfur of a methionine in CT (Met388 in hCT). In T2, this methionine corresponds to Gly418. The sequence changes compensating for the presence of a chloride ion, instead of the SD(Met) atom, are found in each of the T2 sequences. For example, the sequence motif of the Cβ4−Cβ5 loop in each of the T2 sequences, C(413)N(414)GGGG(418)A(419), is uniquely different from the corresponding sequences of the other thiolases (Figure 2), where Asn414 is replaced with a hydrophobic residue and Gly418 with a methionine. The SD(Met) van der Waals contacts with the main chain atoms of the adjacent subunits of CT are in T2 replaced with van der Waals contacts of the corresponding chloride ion (Figure 7).

Catalytic Properties. The active site is shielded from the bulk solvent by the covering loop of the loop domain, and it is only accessible for the substrate via a narrow tunnel shaped by the covering loop and the pantetheine loop (Figures 2 and 6B). The four key catalytic residues protrude out of the four catalytic loops, Cys126, Asn353, His385, and Cys413 (Figure 8). Also present are the catalytic water (Wat98) hydrogen bonded to Asn353, and oxyanion holes 1 and 2. Oxyanion hole 1 is formed by NE2(His353) and Wat98, whereas oxyanion hole 2 is formed by N(Cys126) and N(Gly415) (Figure 8A). The six intermediates of the thiolase reaction cycle and the amino acid residues responsible for the catalysis have been described (*17*, *61*, *65*). The first step in the reaction cycle is the acylation of the cysteine (Cys126 in T2) (Figure 1A). It has been noted that the side chain of this cysteine rotates toward the catalytic histidine (His385 in T2) in the presence of ligand, and this rotation is postulated to be an activation step in which the cysteine is deprotonated by the histidine.

In the apo structure of T2, four waters are found in the catalytic cavity. In the CoA-complexed structure, two waters remain bound in the active site, Wat98 and Wat135 (Figure 8B). Wat135 is weakly hydrogen bonded to the active site water, Wat98. When the apo structure (apoT2) is

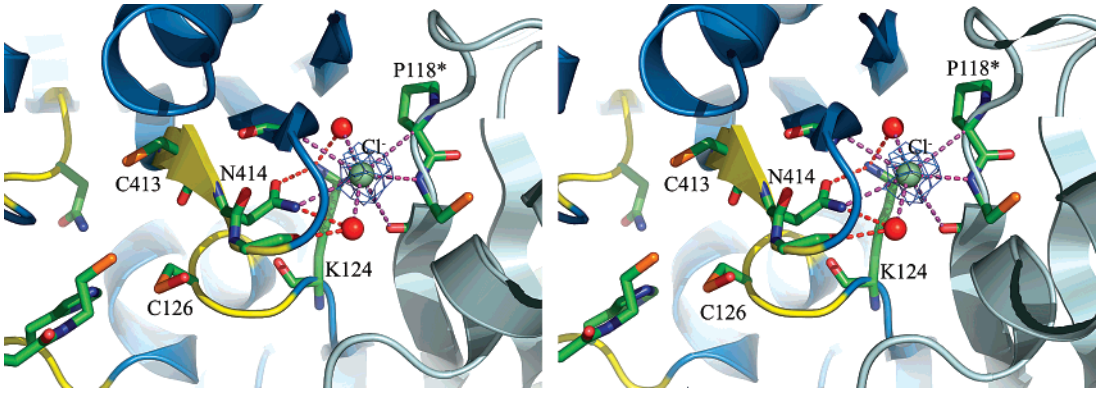

FIGURE 7: Chloride ion binding site at the dimer interface. The active site loops are colored yellow. The interaction partners with the chloride ion (Cl^-) are the residues of the catalytic loops, Nβ3−Nα3 (Lys124) and Cβ4−Cβ5 (Asn414). The red spheres are water molecules via which the bound chloride ion interacts, for instance, with Gly415 of oxyanion hole 2. The chloride ion interacts also with atoms of the Pro118-Cys119 dipeptide of the adjacent monomer (Table 3). The density of the anomalous difference map at the chloride ion (Cl^-) binding site is shown at the 1σ level.

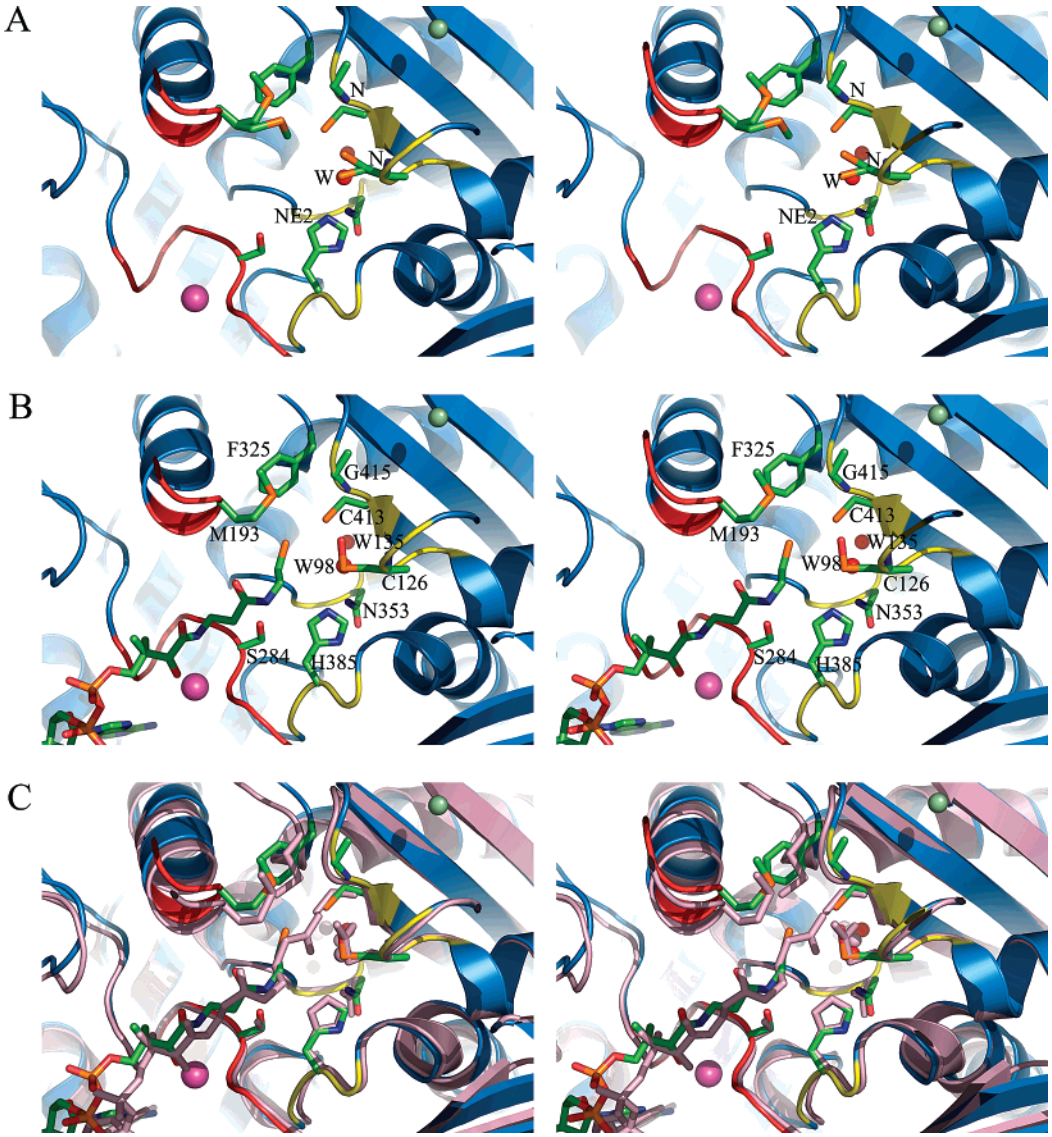

FIGURE 8: Active sites of human T2 and bacterial CT. (A) The active site of apoT2 [PDB entry 2IB8 (this study)]. The atoms of oxyanion hole 1, Wat98 and NE2(His353), and oxyanion hole 2, N(Cys126) and N(Gly415), are highlighted. (B) Active site of T2 in complex with CoA [PDB entry 2IBW (this study)]. The active site cysteine (Cys126) is oxidized. The residues that are labeled, including the catalytic residues (Asn353, His385, and Cys413) of the active site loops (yellow), are discussed in more detail in the text. (C) Superimposition of the liganded active sites of T2 [PDB entry 2IBW (this study)] and bCT [PDB entry 1DM3 (pink color)]. For the superposition calculations, the C_α atoms of the four catalytic loops (*2*) were used. In the bCT structure, the ligand is acetyl-CoA and the catalytic cysteine is acetylated. In every panel, the magenta and green spheres are potassium and chloride ions, respectively.

compared with the liganded structure (T2+CoA), the only structural differences concern side chain rotations of two residues in the active site: Cys126 and Met193 (Figure 8A,B). In the apoT2 structure, the SH group of the active site cysteine, Cys126, has two conformations with equal occupancy as judged from the $2F_o - F_c$ map, and it is not oxidized. In one conformation, SG(Cys126) points toward Gly415 with its χ_1 value of $-23°$ and with a distance from N(Gly415) of 3.4 Å. In the other conformation, SG(Cys126) has rotated approximately 25° toward His385 ($\chi_1 = -47°$) and is now 3.1 Å from NE2(His385). The side chain of Met193 at the active site is also seen to have a double conformation. In the liganded structure (T2+CoA), both Met193 and Cys126 have a fixed position (Figure 8B). The SG atom of Cys126 has adopted the conformation near the His385 side chain, and its sulfur atom is oxidized to a sulfenic acid. Sulfenic acids are unstable entities but can be stabilized by a suitable hydrogen bonding environment (*66*). This extra oxygen atom is located in oxyanion hole 2 that has been identified to be occupied by the thioester oxygen of the acetylated enzyme in complex with acetyl-CoA (*17*). This shows that when the substrate, or a substrate analogue such as CoA, binds in the active site cavity, SG(Cys126) rotates toward NE2(His385) such that the His385 side chain can abstract a proton from Cys126. The thiolate group ($-S^-$) is the nucleophile which reacts with the 3-ketocarbon atom of the substrate to form the covalent intermediate. The thiolate ion is chemically more reactive than the protonated thiol (-SH) group, and the deprotonation of Cys126 makes this sulfur also more susceptible to oxidation. In the T2 structures, the oxidation is seen only in the presence of CoA when SG(Cys126) is in the rotated position close to NE2-(His385). Therefore, the presence of the oxidized cysteine in the liganded structure is in agreement with the notion that this histidine is important for the activation of the catalytic cysteine (*61*).

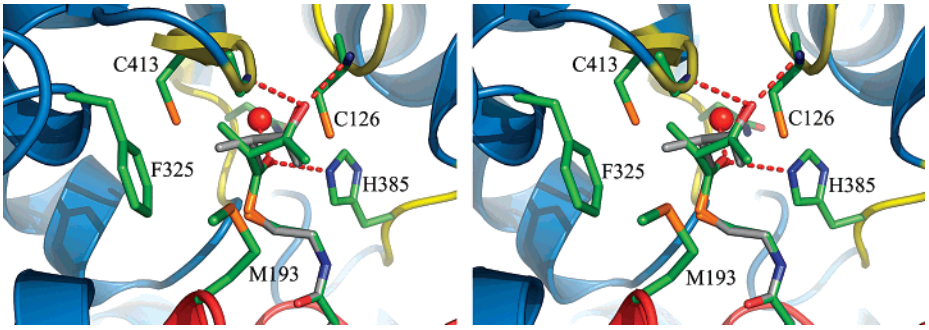

FIGURE 9: Active site of human T2 in the presence of the modeled 2-methylacetoacetyl-CoA. Both enantiomers of 2-methylacetoacetyl-CoA were modeled and are shown as atom-colored skeletons. For clarity, (2*S*)-methylacetoacetyl-CoA is colored gray. The methyl groups of both the 2*S* and 2*R* compound interact with the side chain of Phe325. The thioester oxygen and the 3-keto oxygen atom are located in oxyanion holes 1 and 2, respectively, and the hydrogen bonding interactions are highlighted with red dashed lines. The four catalytic loops with the catalytic residues are colored yellow. Also included in the figure are the side chains of Met193 (which is contacting the ligand) and the four catalytic residues.

When the detailed geometries of the active sites of T2 and CT are compared, two significant differences can be identified, (i) Phe325 (instead of a methionine, Met288 in bCT and Met293 in hCT) and (ii) the absence of a trail of waters extending away from the active site water to the back side of the molecule (*14*). (i) The active sites of T2 and CT are indeed very similar (Figure 8C), except for the occurrence of Phe325 (Figure 8B), which in CT is a methionine. In addition, the residue immediately following the methionine is conservatively replaced with a proline, whereas in CT, the corresponding sequence is a conserved Met-Gly dipeptide (Figure 2). These two residues are at the beginning of helix Cα1 (Figure 2), and the change in these residues causes the catalytic cavity to be narrower in CT than in T2 (Figure 8C). In each of the other available thiolase structures, the corresponding dipeptide is also a Met-Gly dipeptide, in line with the knowledge that each of these thiolases also has as a substrate an unbranched 3-ketoacyl-CoA molecule. The somewhat larger catalytic cavity of T2 correlates with its unique substrate specificity for the 2-methylated acetoacetyl moiety. A modeling exercise on the possible mode of binding of 2-methylacetoacetyl-CoA to this cavity indicates that the 2-methyl group points to the Phe325 side of the cavity (Figure 9). In this docking experiment, guided by the structure of the T2−CoA complex (T2+CoA+KCl, Table 1), the two oxygen atoms of the 2-methylacetoacetyl moiety were positioned near oxyanion holes 1 and 2, as observed in the structure of bCT complexed with acetoacetyl-CoA (*17*). The fit of the 2-methylacetoacetyl moiety in the catalytic cavity is tight; in particular, the ω-acetyl group of the 2-methylacetoacetyl moiety is in close contact with SG-(Cys126). The predicted mode of binding (Figure 9) shows that for both the *R* and *S* forms the 2-methyl group is in van der Waals contact with the Phe325 side chain, consistent with the notion that this T2 unique amino acid residue correlates with the T2 substrate specificity for 2-methylacetoacetyl-CoA. However, such a docking analysis is not sufficient to establish the chiral specificity of the T2 active site. With the mass spectrometry (Figure 3), it is shown that, in the assay, the complete racemic mixture of 2-methylacetoacetyl-CoA is cleaved. In solution, at the high pH of the assay conditions, the *R* and *S* forms of 2-methylacetoacetyl-CoA apparently rapidly interconvert due to the low pK_a of the proton at the 2-position of the 2-methylacetoacetyl moiety (*8*); therefore, further structural binding studies, for example, with inactive variants of T2 complexed with 2-methylacetoaectyl-CoA are required to establish the chiral specificity of the T2 active site. (ii) The other difference in T2 is the absence of a water trail, which is present in CT (*14*, *17*, *61*). The water trail observed in CT is a linear array of hydrogen-bonded waters extending from the active site water to the back side of the molecule. The active site water of this linear array of waters is a hydrogen bonding partner of oxyanion hole 1. This oxyanion hole stabilizes the negative charge as it develops in the catalytic cycle of thiolase. It has been hypothesized that the active site water and its hydrogen bonding network, as observed in CT, could be an important tool in the transition state stabilization of CT (*14*) and, thereby, increase the turnover number. In T2, the active site water (Wat98) is only loosely hydrogen bonded to the neighboring water (Wat135), but this hydrogen bonding network does not extend beyond Wat135 (Figure 8B). In CT, this hydrogen bonding water network is located among Cβ2, Cα2, and Cβ3 of the βαβ unit of the C-terminal half. In T2, these waters are replaced with a cluster of hydrophobic residues: Trp350 (Cβ2), Val352 (Cβ2), Val360 (Cα2), Ile364 (Cα2), and Val374 (Cβ3).

CONCLUDING REMARKS

The crystal structures of T2 show that each T2 subunit has a binding site for a chloride ion and a potassium ion. Each of these ion binding sites is defined well by loops at the active site, resulting in the stabilization of the catalytic loops. From the kinetic data (Table 2), one can see that T2 can degrade acetoacetyl-CoA and 2-methylacetoacetyl-CoA with similar catalytic efficiencies. The comparison of these kinetic data with the published CT data shows that the corresponding turnover numbers for the thiolytic breakdown of acetoacetyl-CoA by CT are approximately 10 times higher than those for T2. Two other key differences between T2 and CT concern the activation of T2 by potassium ions and the unique substrate specificity of T2 which can degrade both acetoacetyl-CoA and 2-methylacetoacetyl-CoA. The latter compound is not a substrate for CT, and CT is not activated by potassium ions. From the comparison of the active site geometries, one can see that the occurrence of the Phe325-Pro326 dipeptide in T2 causes the volume of the catalytic cavity to be larger in T2. Consequently, the 2-methylac-

etoacetyl moiety can bind in the T2 active site, and 2-methylacetoacetyl-CoA can be degraded by T2.

ACKNOWLEDGMENT

We gratefully acknowledge the expert support of the staff of beamlines X11 and BW7A (DORIS storage ring, EMBL/DESY), I711 (MAX II storage ring, MAX-lab), and ID23-1 (ESRF). Furthermore, we thank Ville Ratas for his expert assistance with the purification of the L-3-hydroxyacyl-CoA dehydrogenase, Dr. Kalervo Hiltunen and Dr. Petri Kursula for stimulating discussions, Dr. Annemie Lambert for the expert advice on the kinetic studies, and Dr. Ulrich Bergmann for expert advice with the mass spectrometric measurements. We also gratefully acknowledge the kind gift of the plasmid of human heart short chain L-3-hydroxyacyl-CoA dehydrogenase by Drs. L. J. Banaszak and J. J. Barycki.

REFERENCES

1. Pereto, J., Lopez-Garcia, P., and Moreira, D. (2005) Phylogenetic analysis of eukaryotic thiolases suggests multiple proteobacterial origins, *J. Mol. Evol. 61*, 65−74.
2. Haapalainen, A. M., Meriläinen, G., and Wierenga, R. K. (2006) The thiolase superfamily: Condensing enzymes with diverse reaction specificities, *Trends Biochem. Sci. 31*, 64−71.
3. Gehring, U., and Lynen, F. (1972) Thiolase, in *Enzymes* (Boyer, P. D., Ed.) 3rd ed., pp 391−405, Academic Press, New York.
4. Gehring, U., and Harris, J. I. (1970) The subunit structure of thiolase, *Eur. J. Biochem. 16*, 487−491.
5. Gehring, U., and Harris, J. I. (1970) The active site cysteines of thiolase, *Eur. J. Biochem. 16*, 492−498.
6. Middleton, B. (1973) The oxoacyl-coenzyme A thiolases of animal tissue, *Biochem. J. 132*, 717−730.
7. Middleton, B. (1973) The acetoacetyl-coenzyme A thiolases of rat brain and their relative nactivities during postnatal development, *Biochem. J. 132*, 731−737.
8. Middleton, B., and Bartlett, K. (1983) The synthesis and characterisation of 2-methylacetoacetyl coenzyme A and its use in the identification of the site of the defect in 2-methylacetoacetic and 2-methyl-3-hydroxybutyric aciduria, *Clin. Chim. Acta 128*, 291−305.
9. Fukao, T., Song, X. Q., Mitchell, G. A., Yamaguchi, S., Sukegawa, K., Orii, T., and Kondo, N. (1997) Enzymes of ketone body utilization in human tissues: Protein and messenger RNA levels of succinyl-coenzyme A (CoA):3-ketoacid CoA transferase and mitochondrial and cytosolic acetoacetyl-CoA thiolases, *Pediatr. Res. 42*, 498−502.
10. Fukao, T. (2002) Acetoacetyl-CoA thiolase (cytosolic), in *Wiley encyclopedia of molecular medicine*, pp 5−6, John Wiley & Sons, Inc., New York.
11. Fukao, T. (2002) Acetoacetyl-CoA Thiolase (Mitochondrial), in *Wiley encyclopedia of molecular medicine*, pp 6−9, John Wiley & Sons, Inc., New York.
12. Fukao, T. (2002) Thiolases (Acetyl-CoA acyltransferase), in *Wiley encyclopedia of molecular medicine*, pp 3125−3129, John Wiley & Sons, Inc., New York.
13. Modis, Y., and Wierenga, R. K. (1998) Two crystal structures of N-acetyltransferases reveal a new fold for CoA-dependent enzymes, *Structure 6*, 1345−1350.
14. Kursula, P., Sikkilä, H., Fukao, T., Kondo, N., and Wierenga, R. K. (2005) High resolution crystal structures of human cytosolic thiolase (CT): A comparison of the active sites of human CT, bacterial thiolase, and bacterial KAS I, *J. Mol. Biol. 347*, 189−201.
15. Williams, S. F., Palmer, M. A., Peoples, O. P., Walsh, C. T., Sinskey, A. J., and Masamune, S. (1992) Biosynthetic thiolase from *Zoogloea ramigera*. Mutagenesis of the putative active-site base Cys-378 to Ser-378 changes the partitioning of the acetyl S-enzyme intermediate, *J. Biol. Chem. 267*, 16041−16043.
16. Middleton, B. (1974) The kinetic mechanism and properties of the cytoplasmic acetoacetyl-coenzyme A thiolase from rat liver, *Biochem. J. 139*, 109−121.
17. Kursula, P., Ojala, J., Lambeir, A.-M., and Wierenga, R. K. (2002) The catalytic cycle of biosynthetic thiolase: A conformational journey of an acetyl group through four binding modes and two oxyanion holes, *Biochemistry 41*, 15543−15556.
18. Sambrook, J., Fritzch, E. F., and Maniatis, T. (1989) *Molecular Cloning: A Laboratory Manual*, Cold Spring Harbor Laboratory Press, Plainview, NY.
19. Fukao, T., Yamaguchi, S., Kano, M., Orii, T., Fujiki, Y., Osumi, T., and Hashimoto, T. (1990) Molecular cloning and sequence of the complementary DNA encoding human mitochondrial acetoacetyl-coenzyme A thiolase and study of the variant enzymes in cultured fibroblasts from patients with 3-ketothiolase deficiency, *J. Clin. Invest. 86*, 2086−2092.
20. Niwa, H., Yamamura, K., and Miyazaki, J. (1991) Efficient selection for high-expression transfectants with a novel eukaryotic vector, *Gene 108*, 193−199.
21. Yamaguchi, S., Orii, T., Sakura, N., Miyazawa, S., and Hashimoto, T. (1988) Defect in biosynthesis of mitochondrial acetoacetyl-coenzyme A thiolase in cultured fibroblasts from a boy with 3-ketothiolase deficiency, *J. Clin. Invest. 81*, 813−817.
22. Deng, J., Davies, D. R., Wisedchaisri, G., Wu, M., Hol, W. G., and Mehlin, C. (2004) An improved protocol for rapid freezing of protein samples for long-term storage, *Acta Crystallogr. D60*, 203−204.
23. Jancarik, J., and Kim, S. H. (1991) Sparse matrix sampling: Screening method for crystallization of proteins, *J. Appl. Crystallogr. 24*, 409−411.
24. Zeelen, J. P., Hiltunen, J. K., Ceska, T. A., and Wierenga, R. K. (1994) Crystallization experiments with 2-enoyl-CoA hydratase, using an automated 'fast-screening' crystallization protocol, *Acta Crystallogr. D50*, 443−447.
25. Barycki, J. J., O'Brien, L. K., Bratt, J. M., Zhang, R., Sanishvili, R., Strauss, A. W., and Banaszak, L. J. (1999) Biochemical characterization and crystal structure determination of human heart short chain L-3-hydroxyacyl-CoA dehydrogenase provide insights into catalytic mechanism, *Biochemistry 38*, 5786−5798.
26. Goulart, M. O. F., and Schäfer, H.-Y. (1999) Diastereomeric amides derived from malonic acid: The role of chiral auxiliaries and of the nature of co-acids in the mixed Kolbe electrolyses, *J. Braz. Chem. Soc. 10*, 153−162.
27. Riddles, P. W., Blakeley, R. L., Zerner, B., and Fong, J. C. (1983) Reassessment of Ellman's reagent, *Methods Enzymol. 91*, 49−60.
28. Antonenkov, V. D., Van Veldhoven, P. P., and Mannaerts, G. P. (1999) The commonly used Mg^{2+}-enolate assay can lead to underestimation of thiolase activity, *Anal. Biochem. 267*, 418−420.
29. Thompson, S., Mayerl, F., Peoples, O. P., Masamune, S., Sinskey, A. J., and Walsh, C. T. (1989) Mechanistic studies on β-ketoacyl thiolase from *Zoogloea ramigera*: Identification of the active-site nucleophile as Cys89, its mutation to Ser89, and kinetic and thermodynamic characterization of wild-type and mutant enzymes, *Biochemistry 28*, 5735−5742.
30. Kabsch, W. (1993) Automatic processing of rotation diffraction data from crystals of initially unknown symmetry and cell constants, *J. Appl. Crystallogr. 26*, 795−800.
31. Kursula, P. (2004) XDSi: A graphical interface for the data processing program XDS, *J. Appl. Crystallogr. 37*, 347−348.
32. Matthews, B. W. (1968) Solvent content of crystals, *J. Mol. Biol. 33*, 491−497.
33. Vagin, A., and Teplyakov, A. (1997) MOLREP: An automated program for molecular replacement, *J. Appl. Crystallogr. 30*, 1022−1025.
34. Brünger, A. T. (1998) Crystallography, and NMR system: A new software system for macromolecular structure determination, *Acta Crystallogr. D54*, 905−921.
35. Perrakis, A., Morris, R., and Lamzin, V. S. (1999) Automated protein model building combined with iterative structure refinement, *Nat. Struct. Biol. 6*, 458−463.
36. Murshudov, A., Vagin, A., and Dodson, E. J. (1997) Refinement of Macromolecular Structures by the Maximum-Likelihood Method, *Acta Crystallogr. D53*, 240−255.
37. Jones, T. A., Zou, J. Y., Cowan, S. W., and Kjeldgaard, M. (1991) Improved methods for binding protein models in electron density maps and the location of errors in these models, *Acta Crystallogr. A47*, 110−119.
38. Laskowski, R. A., McArthur, M. W., Moss, D. S., and Thornton, J. M. (1993) PROCHECK: A program to check the stereochemical quality of protein structures, *J. Appl. Crystallogr. 26*, 283−291.

39. Vriend, G. (1990) WHAT IF: A molecular modeling and drug design program, *J. Mol. Graphics 8*, 52−56.
40. Merritt, E. (2006) http://www.bmsc.washington.edu/people/merritt/.
41. Schuettelkopf, A. W., and van Aalten, D. M. F. (2004) PRODRG: A tool for high-throughput crystallography of protein-ligand complexes, *Acta Crystallogr. D60*, 1355−1363.
42. DeLano, W. L. (2002) *PyMOL*, DeLano Scientific, San Carlos, CA.
43. Clinkenbeard, K. D., Sugiyama, T., Moss, J., Reed, W. D., and Lane, M. D. (1973) Molecular and catalytic properties of cytosolic acetoacetyl coenzyme A thiolase from avian liver, *J. Biol. Chem. 248*, 2275−2284.
44. Harding, M. M. (2002) Metal-ligand geometry relevant to protein and in proteins: Sodium and potassium, *Acta Crystallogr. D58*, 872−874.
45. Di Cera, E. (2006) A structural perspective on enzymes activated by monovalent cations, *J. Biol. Chem. 281*, 1305−1308.
46. Kowaltowski, A. J., Cosso, R. G., Campos, C. B., and Fiskum, G. (2002) Effect of Bcl-2 overexpression on mitochondrial structure and function, *J. Biol. Chem. 277*, 42802−42807.
47. Liu, D., Slevin, J. R., Lu, C., Chan, S. L., Hansson, M., Elmer, E., and Mattson, M. P. (2003) Involvement of mitochondrial K^+ release and cellular efflux in ischemic and apoptotic neuronal death, *J. Neurochem. 86*, 966−979.
48. Zoeteweij, J. P., van de Water, B., de Bont, H. J., and Nagelkerke, J. F. (1994) Mitochondrial K^+ as modulator of Ca^{2+}-dependent cytotoxicity in hepatocytes. Novel application of the K^+-sensitive dye PBFI (K^+-binding benzofuran isophthalate) to assess free mitochondrial K^+ concentrations, *Biochem. J. 299*, 539−543.
49. Costa, A. D., Quinlan, C. L., Andrukhiv, A., West, I. C., Jaburek, M., and Garlid, K. D. (2006) The direct physiological effects of mitoK(ATP) opening on heart mitochondria, *Am. J. Physiol. 290*, H406−H415.
50. Chavez, E., Moreno-Sanchez, R., Zazueta, C., Reyes-Vivas, H., and Arteaga, D. (1991) Intramitochondrial K^+ as activator of carboxyatractyloside-induced Ca^{2+} release, *Biochim. Biophys. Acta 1070*, 461−466.
51. Garlid, K. D. (1978) Unmasking the mitochondrial K/H exchanger: Swelling-induced K^+-loss, *Biochem. Biophys. Res. Commun. 83*, 1450−1455.
52. Garlid, K. D. (1980) On the mechanism of regulation of the mitochondrial K^+/H^+ exchanger, *J. Biol. Chem. 255*, 11273−11279.
53. Inoue, I., Nagase, H., Kishi, K., and Higuti, T. (1991) ATP-sensitive K^+ channel in the mitochondrial inner membrane, *Nature 352*, 244−247.
54. Siemen, D., Loupatatzis, C., Borecky, J., Gulbins, E., and Lang, F. (1999) Ca^{2+}-activated K channel of the BK-type in the inner mitochondrial membrane of a human glioma cell line, *Biochem. Biophys. Res. Commun. 257*, 549−554.
55. Szabo, I., Bock, J., Jekle, A., Soddemann, M., Adams, C., Lang, F., Zoratti, M., and Gulbins, E. (2005) A novel potassium channel in lymphocyte mitochondria, *J. Biol. Chem. 280*, 12790−12798.
56. Otto, D. A., and Ontko, J. A. (1982) Structure-function relations between fatty acid oxidation and the mitochondrial inner-membrane matrix region, *Eur. J. Biochem. 129*, 479−485.
57. Halestrap, A. P., and Armston, A. E. (1984) A re-evaluation of the role of mitochondrial pyruvate transport in the hormonal control of rat liver mitochondrial pyruvate metabolism, *Biochem. J. 223*, 677−685.
58. Halestrap, A. P., and Dunlop, J. L. (1986) Intramitochondrial regulation of fatty acid β-oxidation occurs between flavoprotein and ubiquinone. A role for changes in the matrix volume, *Biochem. J. 239*, 559−565.
59. Pawelczyk, T., Easom, R. A., and Olson, M. S. (1988) The effects of various anions and cations on the regulation of pyruvate dehydrogenase complex activity from pig kidney cortex, *Biochem. J. 253*, 819−825.
60. Ciszak, E. M., Korotchkina, L. G., Dominiak, P. M., Sidhu, S., and Patel, M. S. (2003) Structural basis for flip-flop action of thiamin pyrophosphate-dependent enzymes revealed by human pyruvate dehydrogenase, *J. Biol. Chem. 278*, 21240−21246.
61. Modis, Y., and Wierenga, R. K. (2000) Crystallographic analysis of the reaction pathway of *Zoogloea ramigera* biosynthetic thiolase, *J. Mol. Biol. 297*, 1171−1182.
62. Denessiouk, K. A., and Johnson, M. S. (2003) "Acceptor-donor-acceptor" motifs recognize the Watson-Crick, Hoogsteen and Sugar "donor-acceptor-donor" edges of adenine and adenosine-containing ligands, *J. Mol. Biol. 333*, 1025−1043.
63. Dauter, Z., Dauter, M., de La Fortelle, E., Bricogne, G., and Sheldrick, G. M. (1999) Can anomalous signal of sulfur become a tool for solving protein crystal structures? *J. Mol. Biol. 289*, 83−92.
64. Steiner, T. (1998) Hydrogen-bond distances to halide ions in organic and organometallic crystal structures: Up-to-date database study, *Acta Crystallogr. B54*, 456−463.
65. Modis, Y., and Wierenga, R. K. (1999) A biosynthetic thiolase in complex with a reaction intermediate: The crystal structure provides new insights into the catalytic mechanism, *Structure 7*, 1279−1290.
66. Claiborne, A., Yeh, J. I., Mallett, T. C., Luba, J., Crane, E. J., III, Charrier, V., and Parsonage, D. (1999) Protein-sulfenic acids: Diverse roles for an unlikely player in enzyme catalysis and redox regulation, *Biochemistry 38*, 15407−15416.
67. Kabsch, W., and Sander, C. (1983) Dictionary of protein secondary structure: Pattern recognition of hydrogen-bonded and geometrical features, *Biopolymers 22*, 2577−2637.

BI6026192